FLOW AND SUSPENDED SEDIMENT TRANSPORT THROUGH THE GRAVEL-SAND TRANSITION IN THE FRASER RIVER, BRITISH COLUMBIA

by

Natalia Domarad
Bachelor of Science, University of Toronto

THESIS SUBMITTED IN PARTIAL FULFILLMENT OF
THE REQUIREMENTS FOR THE DEGREE OF

MASTER OF SCIENCE

In the
Department of Geography

SIMON FRASER UNIVERSITY

Spring 2011

APPROVAL

Name: **Natalia Domarad**

Degree: **Master of Science**

Title of Thesis: **Flow And Suspended Sediment Transport Through The Gravel-Sand Transition In The Fraser River, British Columbia**

Examining Committee:

Chair: **Eugene McCann**
Associate Professor

_____

Jeremy G. Venditti
Senior Supervisor
Assistant Professor

_____

Edward J. Hickin
Supervisor
Professor Emeritus

_____

Michael Bliss Singer
External Examiner
Lecturer
University of St. Andrews

Date Defended/Approved: 21 April 2011

Declaration of
Partial Copyright Licence

ABSTRACT

The Fraser River, British Columbia is a large alluvial channel that features an abrupt gravel-sand transition that occurs due to a dramatic slope change and the ocean base-level control. There have been no previous observations of the sediment dynamics through transitions in rivers of this scale. I examine the spatial and temporal changes in flow and the suspended sediment transport regime through the transition using hydro-acoustics in an attempt to test the hypothesis that sand in the gravel-bedded reach is coming out of suspension to form the sand-bedded reach. The results indicate that during high flows a downstream shear stress gradient does not exist and the suspended sediment flux declines downstream until the sand-bedded reach where the flux increases. These results suggest that there is a sediment supply gradient and during low flows sand is stored in the gravel-bedded reach and only released to the sand-bedded reach during large floods.

Keywords: Fraser River; gravel-sand transition; suspended-sediment transport; sediment dynamics; ADCP; LISST.

ACKNOWLEDGEMENTS

I would like to offer my gratitude and appreciation to my committee: Dr. Jeremy Venditti, Dr. Ted Hickin, Dr. Michael Singer, and Dr. Eugene McCann. A special thanks to Dr. Venditti for providing knowledgeable insight into this work, and allowing me the space to learn on my own. Thank you to those who have helped in the field especially: Dr. Mike Church, Dr. Ray Kostaschuk, Megan Hendershot, Robert Humphries, Martin Lin, Jordan MacDonald and Sally Haggerstone.

Finally, I would like to thank my parents, along with Joey and Fish, and Mantle for their understanding and support.

TABLE OF CONTENTS

LIST OF FIGURES

LIST OF TABLES

1: GENERAL INTRODUCTION AND LITERATURE REVIEW

1.1 Introduction

Many river systems exhibit significant downstream fining, especially if there are few inputs of coarse sediments from tributaries or valley walls. This downstream fining tendency is a fundamental control in rivers because the size of bed material significantly influences sediment transport, flow resistance, and channel morphology (Knighton, 1998). The downstream fining of bed sediment, however, is not always a spatially gradual process. Discontinuities can occur such as the gravel to sand transition, where an abrupt change in bed sediment from gravel (through a short bimodal reach) to an entirely sand bed has been observed in some rivers (Sambrook Smith and Ferguson, 1995).

The abruptness of these transitions suggests that they are not simply an extension of downstream fining, but rather a threshold between different types of rivers (Howard, 1980). Gravel-bedded and sand-bedded rivers are seen as distinct by geomorphologists, sedimentologists, ecologists, and river engineers (Ferguson, 2003), with different sediment transport processes dominating each of these river types. Gravel bedded channels are threshold channels, where the full bed material grain-size distribution is mobile at high flows. Sand bedded channels, on the other hand, are labile with bed material that can be moved even by low flows.

It has been suggested that the mechanisms that cause the gravel-sand transition are a combination of abrasion, a nonconservative mechanism where large clasts become smaller through surface attrition or breakage, and size-selective transport and deposition. Gravel to sand transitions occur most commonly where relatively steep mountain rivers emerge into wide valleys or plains with much lower slope, and the reduction in fluid shear stress forces the river to deposit most of its bedload (Ferguson, 2003). Sediment supply has also been linked to gravel-sand transitions and downstream fining especially where there are large inputs of fine sediment (Brierley and Hickin, 1985; Ferguson, 1995; Knighton, 1998). Research on gravel to sand transitions has generally focused on small drainage basins (e.g. Ferguson et al., 1996; Seal and Paola, 1995) and it is unknown if this research applies to larger basins. In addition, few studies have examined sediment transport processes; more specifically, gradients in suspended sediment that must occur in large channels to create the sand bed.

In many channels, sand and gravel can be carried as bedload and the transition occurs where the gravel cannot be carried any further downstream because of hydraulic incompetence or when fines are in abundance. In some channels, sand is carried as suspended load through the gravel-bedded portions of the channel and deposition from suspension causes the transition. In both cases the suspended-sediment concentration and shear stress gradients control the patterns of grain-size change.

Previous work (Venditti et al., 2010c; McLean et al., 1999) suggests that the Fraser River transition is caused by a lack of competence causing sand to come out of suspension to form sand patches on the bed and that general gravel motion ceases. This suggestion is tested here by measuring flow and suspended sediment for the gravel-sand transition reach and examining sediment dynamics and how they influence the transition.

1.2 Literature Review

Gravel-sand transitions are characterized by an abrupt change in bed sediment from gravel to an entirely sand bed. Figure 1 illustrates this process for the Allt Dubhaig, a stream (~10 m wide) in the Central Highlands of Scotland (Sambrook Smith and Ferguson, 1996). The upstream end is entirely gravel-bedded and becomes increasingly bimodal downstream. Sorting patterns cause the gravel to deposit in pools and sand to deposit in bar tails. The median grain size decreases rapidly although gravel movement does not completely cease and a diminishing veneer of fine gravel can be found in deep pools. The transition area behaves like a sequence of meander bends, with high-energy flow at the outside of bends crossing downstream to the outside of the next bend.

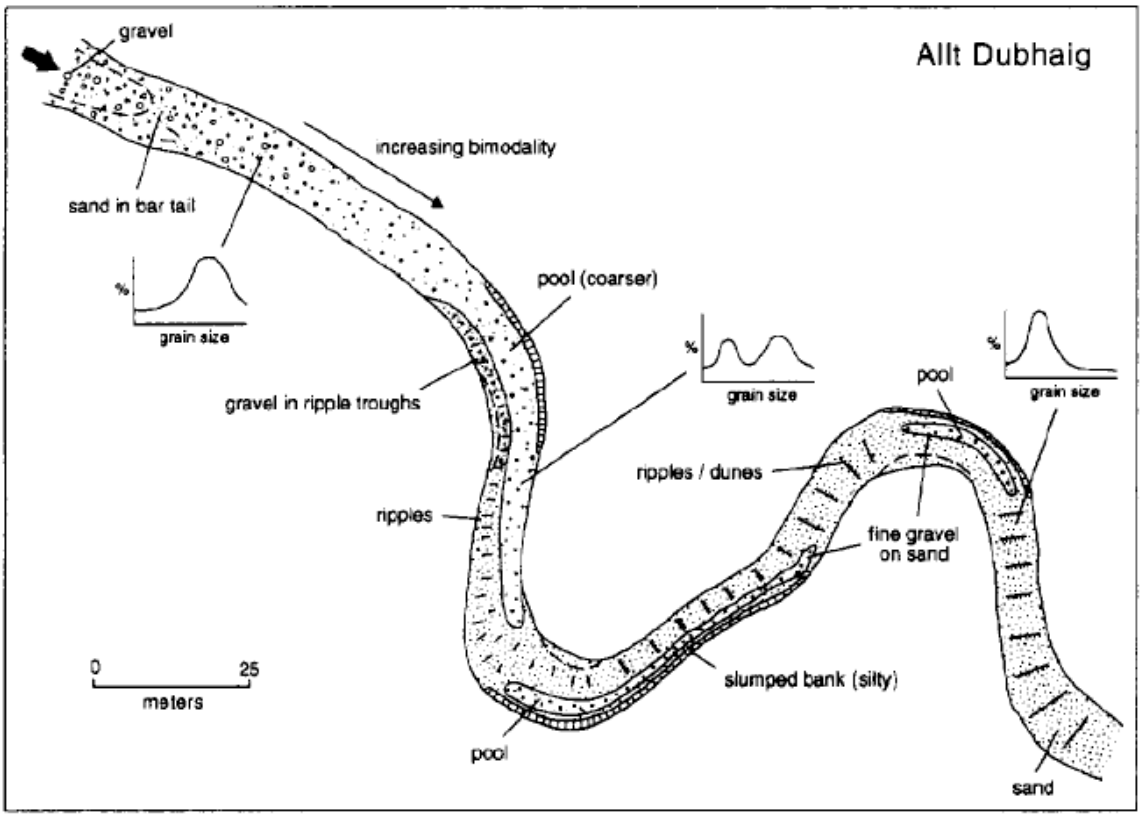

Figure 1: Main features of the gravel to sand transition of the Allt Dubhaig, Scotland (Sambrook Smith and Ferguson, 1995).

The mechanisms suggested in the literature as the cause of these transitions are a combination of: (1) abrasion; (2) selective transport and deposition; (3) base-level change; and (4) sediment supply controls (Sambrook Smith and Ferguson, 1995).

1.2.1 Abrasion/Breakdown

Yatsu (1955) examined downstream fining of bed sediments in the Kinu River in Japan. Figure 2 illustrates downstream fining and a gravel-sand transition in the Kinu River. Yatsu argued that rapid gravel-sand transitions are caused by the tendency for sediment in the range of 2-4mm to be crushed into

smaller grains. However, Yatsu (1955) did not provide direct evidence that the actual breakdown of the sediment was occurring.

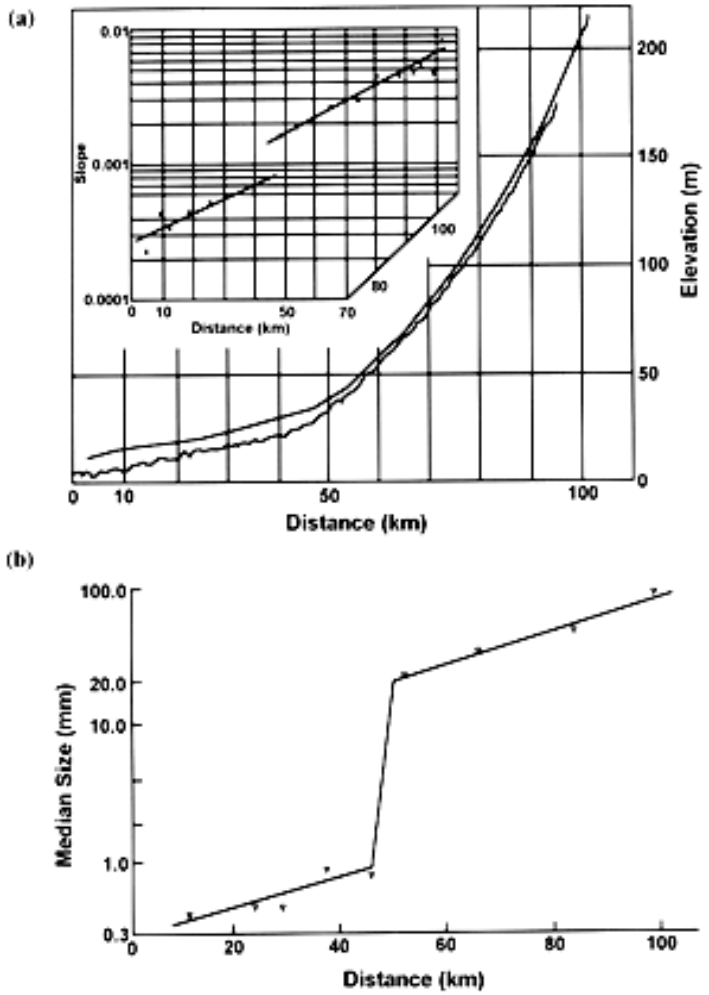

Figure 2: Long profile (a) and downstream change in grain size (b) of the Kinu River, Japan (Yatsu, 1955).

Kodama (1994) documented downstream fining by particle abrasion in tumbling mill experiments and examined the lithology of bed material along the Waterase River, Japan. This study provided field evidence that suggests particle abrasion does occur in the field and is responsible, at least in part, for the downstream decrease in particle size of bed material. The results indicate that

the size distribution of gravel is strongly related to the lithology, as the longitudinal changes in the lithologic composition of each grain size class suggest that selective transport by lithology occurs in every gravel size fraction. These results (Figure 3) show the downstream changes in particle size and the weight percentage (determined by dividing all sieved samples larger than 16mm into four categories) and lithologic composition by weight of each grain size at every sampling site (1-9).

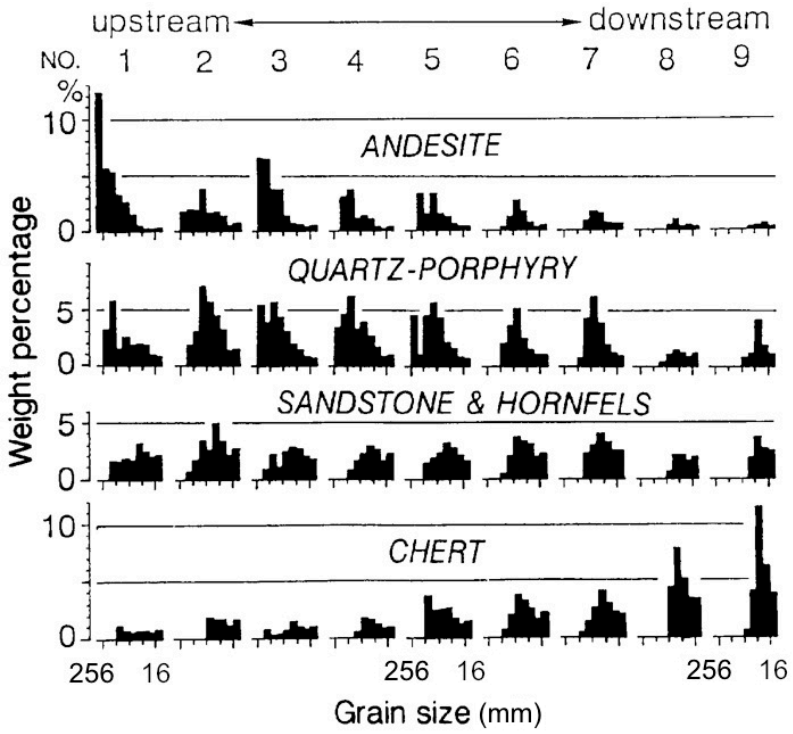

Figure 3: Downstream changes in particle size of different lithologies in the Waterase River (modified slightly from Kodama, 1994).

In addition, this study notes that abrasion dominates in degrading river systems. In aggrading systems the coarse particles may have few chances to be moved and become increasingly buried. Kodama (1994) suggested that the

mobility of particles in any size class is influenced by particle shape; for example, chert particles are usually more angular and may be more difficult to transport.

Shaw and Kellerhals (1982) provided a large data set which consisted of 174 samples from rivers with maximum discharges of ~5000 m^3s^{-1} and depths under 5 m. Shaw and Kellerhals (1982) also observed enhanced breakdown of particular grain sizes and concluded that 1-4mm material is readily crushed to produce finer material that can be carried in suspension. They also hypothesized that once the bed D50 is between 8-16mm a rapid transition to sand occurs because these sizes can be preferentially transported across the smoother bed surface. This increased transport leads to more abrasion of gravel, and more production of sand, until ultimately a fully sand-bedded river forms. Kodama (1994) and Sambrook Smith and Ferguson (1995) also argued that abrasion is probably important in large-scale, higher-energy rivers. Based on the literature it is clear that strong lithologic controls are required for abrasion to dominate.

1.2.2 Sorting and Selective Transport

Gravel-sand transitions are most common where steep mountain rivers emerge onto valleys or plains with much lower slope, and the reduction in fluid shear stress forces the river to deposit most of its bedload (Ferguson, 2003). The abruptness of gravel-sand transitions is largely associated with a break in slope where the maximum size of sediment that can be transported is reduced (Sambrook Smith and Ferguson, 1995).

Brierley and Hickin (1985) observed downstream fining in the Squamish River, British Columbia by examining the size of gravel on channel bars, and concluded that particle size change is described by a power function and not by the exponential relationship proposed by Sternberg (1875). They suggest decline in particle size is likely the result of selective transport based on competence and capacity based sorting. Ferguson (2003) suggests that sorting is enhanced as the differences in critical shear stress to move different grain sizes becomes relatively greater as shear stress declines downstream. This creates a series of positive feedbacks. First, the preferential mobility of smaller grain sizes increases, so bedload becomes much finer than the bed. Then as this fine bedload is deposited downstream, the bed becomes increasingly finer so that subsequent bedload is still finer because of the reduced availability of coarse fractions. Finally, once the deposited load contains >30% sand, it forms sand patches and eventually a continuous sand matrix with embedded or over-passing gravel, which further increases the effective availability of sand. The last of these feedbacks was invoked by Wilcock (1998), who speculated that preferential mobility of sand could trigger abrupt gravel to sand transitions.

Ferguson (2003) created a numerical model that simulates bed aggradation or degradation, and fining or coarsening, using finite-difference versions of the standard overall (Exner) and fractional (Hirano) sediment continuity equations. In Ferguson's model the bed consists of a gravel and sand mixture; the initial sand fraction varies linearly downstream and the initial slope declines linearly downstream. Water is fed to the model at a specified unit

discharge *q* and local shear stress is calculated from *q* and slope using the Manning equation. Gravel and sand are fed to the model at capacity rates so that the bed at 0 km downstream does not aggrade or degrade.

The results of this model support the hypothesis that preferential mobility of sand can cause the development of strong downstream fining where little or none existed originally, as long as the slope decreases downstream and fining becomes concentrated into a zone of abrupt increase of the sand fraction. Ferguson (2003) concludes that nonlinearities in bedload transport and deposition mechanisms can cause an abrupt gravel to sand transition to develop, without any contribution by abrasion, as downstream changes in bed composition are amplified by a strong decline in shear stress.

1.2.3 Local Base-Level Control

Local base-level control is seen as a common feature in rivers that exhibit rapid downstream fining. In their review of possible causes and mechanisms of gravel-sand transitions, Sambrook-Smith and Ferguson (1995) propose local base-level as a cause. They indicate that all channels they studied have a rapid change in water-surface slope caused by a local base-level control (such as a dam, lake, debris fan, main channel, or ocean). They explain that these local controls reduce river competence and induce deposition, reducing the sediment load and grain size by selective deposition. This results in only sand being mobile, which congests the remaining gravel until a sand bed forms within a short distance. This can be seen in Figure 4, which illustrates the change in water-

surface slope downstream with the changes in D_{50} for Beauty Creek, Alberta (Sambrook Smith and Ferguson, 1995).

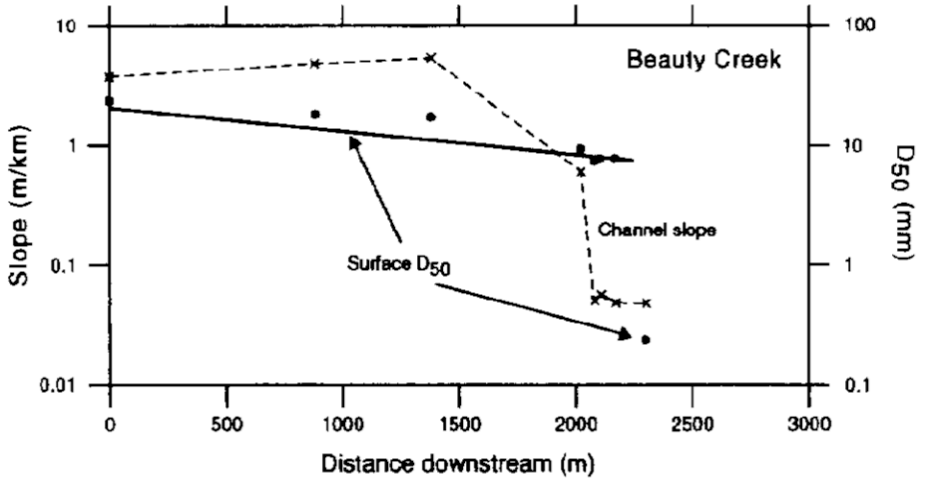

Figure 4: Changes in water-surface slope with associated changes in median grain-size for Beauty Creek, Alberta (Sambrook Smith and Ferguson, 1995).

Pickup (1984) also used local base-level control to explain the changing position of gravel-sand transitions in the Fly and Purari Rivers in Papua New Guinea. He suggested that the sea level was once lower and the gradient through what is now the transition reach was greater and capable of transporting both gravel and sand supplied to it. The rise in sea-level reduces slope, resulting in gravels being left as a lag that rarely moves and more sand is therefore being deposited. This allows the transition reach to become fully sand-bedded due to the supply of only sand and the low slopes downstream.

Sambrook-Smith and Ferguson (1996) used flume experiments with bimodal sediment feed to investigate the changes associated with transitions caused by the effects of a local base-level control. Their results can be used to predict the spatial sequence of situations likely to occur along a concave long

profile above a local base level. They indicate that deposition was size-selective and led to the following sequence of bed texture change as slope decreased: (1) sand in lee of gravel clusters, (2) elongated sandy patches and thin streaks, and (3) wider sand ribbons covering gravel completely and developing ripples. In addition, they suggest that this sequence can be interpreted as a set of temporal changes that would be expected in a channel that was aggrading and reducing its slope as a result of a rise in local base level.

The mechanisms behind these temporal changes and spatial sequence are given below. At first, as the slope is reduced, the material in transport becomes finer and is apparent on the bed in the lee of pebble clusters, where small sand tails appear. These localized sand patches are too small to alter the flow. However, as the slope decreases they elongate into longitudinal sand ribbons. This does affect the flow, as the near bed velocities are much greater than over adjacent gravel sections. Further decline in slope results in a predominantly sand surface with the coarsest gravel particles still visible, which causes the flow to adjust completely to this change in grain size. A final reduction in slope enables the coarsest particles to become buried and the bed becomes fully sand-bedded. The flow adjusts to this smooth surface as the near-bed velocity increases and the average shear stress decreases.

1.2.4 Sediment Supply

Sambrook-Smith and Ferguson (1995) propose that sediment supply, specifically, large inputs of fine sediment can control abrupt gravel to sand transitions. A study by Seal and Paola (1995) emphasizes the role of

downstream sorting as a response to changes in sediment supply. They examined the North Fork Toutle River in Washington where fine sediment supply is abundant resulting in a short length of the depositional system and rapid aggradation rates implying selective deposition.

Work by Campbell (1970) investigated the Red Deer River, which flows through the Alberta badlands near Drumheller where the gravel-sand transition occurs. These badlands contribute significant amounts of clay, silt and fine to medium sand to the Red Deer River, because the sediment is eroded after small, localized, high-intensity storms. Therefore, it is likely that there is an excess of sand input, which clogs and buries the gravel to form a sand bed. This stored sand remains because the river can only transport it during rare events.

Knighton (1998) discusses a gravel-sand transition in a disturbed catchment in the Ringarooma River, Tasmania, where more than 40 million cubic metres of mining waste were supplied to the river between 1875 and 1984. Knighton proposed that this input of mining waste induced a sharp gravel-sand transition in which median grain size decreased from over 30mm to 3mm in less than 500m. The transition has been in the same location for 12 years although it is projected to propagate downstream with a lack of fine sediment input.

A study by Singer (2008) linked sediment supply to changes in material grain size in the Sacramento River. Singer proposed that anthropogenic sediment supply reduction due to dam installation and extensive aggregate mining may result in coarsening at the edges of the channel, a finer ‘ribbon’ of active sediment transport, a stranding of bars, and bed patchiness, all of which

would influence longitudinal patterns of downstream fining. In addition, Singer (2010) investigated bathymetry, modelled flow, and sediment flux in the same field site, the Sacramento River. The results suggested that following the sediment supply decline and a shift to a finer sediment supply, the gravel-sand transition in the Sacramento River extended and migrated upstream. Singer (2010) also suggested that the gravel-sand transition is probably an emergent phenomenon (Ferguson, 2003), but it can be obscured by transience in sediment transport response to changes in supply.

1.2.5 Synthesis

Currently it is known that abrasion, sorting and patchiness are the main processes responsible for downstream fining. The gravel-sand transition is more likely caused by sorting, base-level control, and sediment supply, as strong lithologic controls are required for abrasion to dominate. Literature examining gravel to sand transitions has previously focused on laboratory experiments in flumes and small channels where transitions occur very abruptly over short distances (Paola and Seal, 1995; Sambrook Smith and Ferguson, 1995; Ferguson, 2003). Most detailed studies have focused on rivers with depths of less than 5 m and widths less than 40 m. Other studies examining larger rivers (Gomes, 2001; Knighton 1989; Singer, 2008; 2010) have different controls such as low sediment supply caused by anthropogenic impact.

In addition, many studies have developed or used models to predict the gravel-sand transition and downstream fining which have been tested against small rivers such as the Allt Dubhaig in Scotland (Ferguson, 2003) and the North

Fork Toutle River in Washington (Seal and Paola, 1995). This may be of concern, as processes that dominate at small-scales may not dominate at much larger scales. Larger rivers offer the potential for more spatial variability and have the width to accommodate that variability and greater transport capacity. Therefore, it is important to make sure that the transport processes dominating in small scale channels dominate in larger scale channels.

This study builds on work by Venditti et al. (2010c), which examined the gravel-sand transition in Fraser River, British Columbia. Previous work on the Fraser had suggested that the gravel-sand transition reach occurs between Yaalstrick Bar and Mission where there is a reduction in gradient from 2×10^{-4} in the Chilliwack reach upstream of Yaalstrick Bar to 6×10^{-5} at Mission (McLean et al., 1999). In the gravel-bedded reach upstream of Yaalstrick Bar the channel bed is mostly comprised of strongly bimodal sediment consisting of gravel as the coarse fraction (median diameter in the range of 25-30 mm), and medium sand as the fine fraction (0.3 mm); sand comprises roughly 10-20% of the bed material (McLean et al., 1999). The river exhibits an abrupt change from a wandering gravel multiple-channel planform to a single-thread, sand-bedded channel planform near the town of Mission, at Sumas Mountain.

The work by Venditti et al., (2010c) confirmed that the river bed at Yaalstrick Bar is comprised of gravel and that sand is carried in suspension. At Mission, the bed is entirely sand bedded. This work suggests that sorting patterns between Yaalstrick Bar and Mission, caused by the superior mobility of gravel over sand (the tendency for gravel to be carried over sand patches in the

transport process), have lead to gravel patches through the apex of some river bends and gravel bar heads, but the rest of the channel bed is sand. In addition, they propose that the bedforms associated with sand-gravel mixtures appear in a sequence (sand ribbons, barchans, dunes) on the riverbed immediately downstream of Yaalstrick Bar, suggesting sand deposition from suspension. However, extensive gravel deposits do not occur downstream of Yaalstrick Bar, suggesting the transition is abrupt and occurs at the downstream end of Yaalstrick Bar. This is supported by a dramatic increase in bar amplitude downstream of Yaalstrick Bar, implying greater sand composition (Venditti et al., 2010c).

The results of Venditti et al. (2010c) further suggest that the strongest control on the location of the gravel-sand transition is a loss of competence, which is thought to cease gravel transport and allow sand to come out of suspension. As such, there should be strong gradients in gravel mobility downstream of Yaalstrick Bar. There should also be strong gradients in suspended-sediment transport and grain size from Yaalstrick Bar to Mission.

1.3 Research Objectives and Hypothesis

This research seeks to understand the following questions: (1) What are the dominant sediment transport processes in the transition reach of the Fraser River? (2) Are there downstream gradients in shear stress that lead to reduced gravel mobility downstream of Yaalstrick Bar? (3) Are there downstream gradients in suspended-sediment flux that demonstrate deposition from suspension? The specific objectives are to:

1. Investigate spatial and temporal changes in flow depth, velocity, and shear stress throughout the gravel-sand transition reach;
2. Examine spatial changes in the suspended sediment transport regime at high and low flows throughout the transition reach;
3. Explore downstream gravel and sand mobility comparing observed spatial shear stress patterns to the shear stress required to entrain gravel into bedload and sand into suspension.

2: FIELD SITE

My field site is the gravel-sand transition in the Fraser River, British Columbia. The Fraser River drains an area of 228 000 km^2 from the Rocky Mountains through the sub-humid Interior Plateau to the humid Coast Range into the Strait of Georgia. When the river emerges from the Rocky Mountains it enters a 270 km bedrock canyon, it then exits the Fraser Canyon into the lower portion of the river where it becomes alluvial and begins to deposit its gravel load roughly 190 km upstream from the sea. From Hope, BC, which is located at river km (RK) 165, the river undergoes a 10x reduction in water-surface slope (Figure 5), where bed conditions change from gravel to sand.

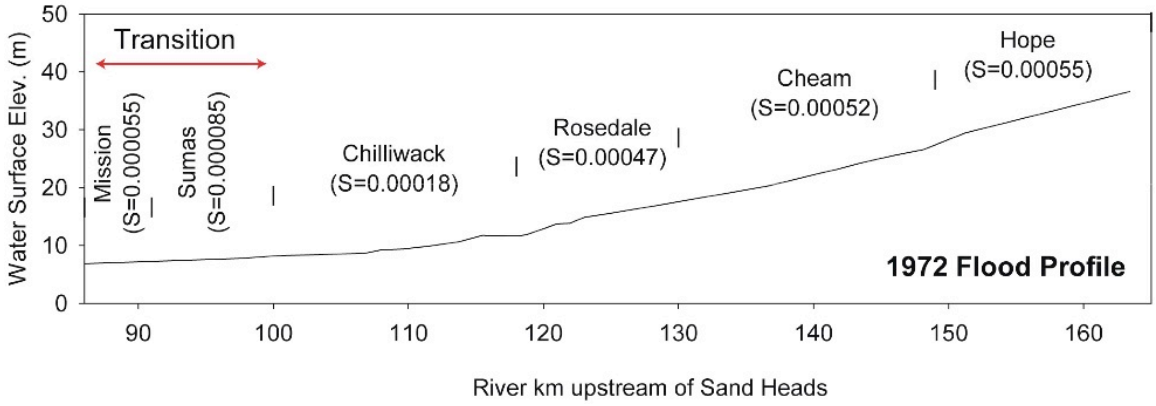

Figure 5: Water surface elevation of the 1972 Fraser River flood profile. Surface slopes (S) are provided and 'transition' marks the reaches (Mission and Sumas) where the gravel-sand transition is thought to occur (Venditti et al., 2010c based on McLean, 1990).

2.1 Hydrology of the Fraser River

Flows in the Fraser River are dominated by a single event hydrograph that is primarily controlled by snowmelt. Figure 6 shows the average annual hydrograph at Mission gauging station (Water Survey of Canada Station ID: 08MH024) with mean, minimum, and maximum flows from January 1965 to December 2009. Minimum flows for the Fraser River occur from late November to April and peak flows dominate from late May to early July. Mean annual flow at Mission is 3410 m^3s^{-1}, the mean annual flood is 9790 m^3s^{-1}, and the largest measured flood of record was 15,200 m^3s^{-1} in 1948 at Hope. The stage-discharge relation at Mission is complex due to tidal influences. The Water Survey of Canada (WSC) estimates flows from a regression model using discharge from the Hope gauging station (WSC Station ID: 08MF005) and tidal elevations at Point Atkinson located near the mouth of the river in the Strait of Georgia. Tides influence water levels below Sumas Mountain and the tidal range varies from a few centimetres during the freshet to >1 metre during the winter causing diurnal fluctuations of a few hundred to 1000 m^3s^{-1} in discharge at Mission during peak flows (McLean et al., 1999).

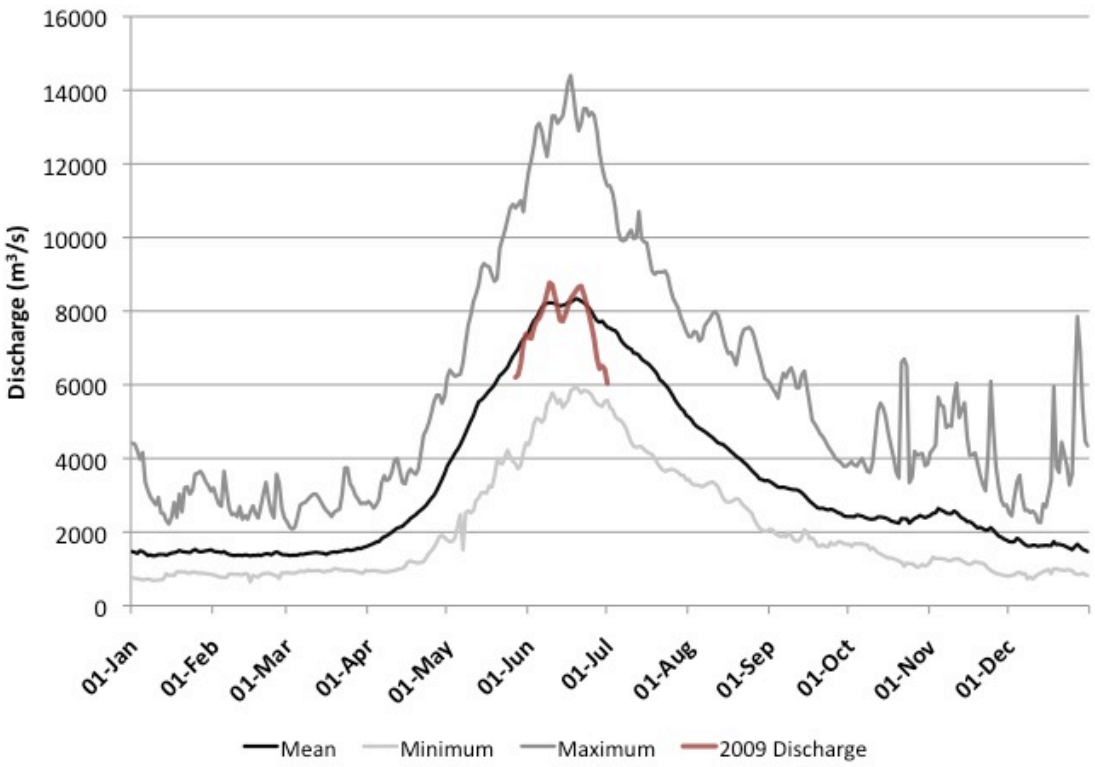

Figure 6: Average annual hydrograph for Fraser River at Mission (data source: WSC).

2.2 Characteristics of sediment transport in lower Fraser River

The Lower Fraser River begins where it exits the Fraser Canyon in Yale, BC and extends 190 km to the sea (Figure 7). The WSC conducted a comprehensive sediment transport measurement program between 1965 and 1987 at several locations on the Lower Fraser River. Mclean et al. (1999), presented these data in an overall assessment of the measurement program, and some of the results are summarized here.

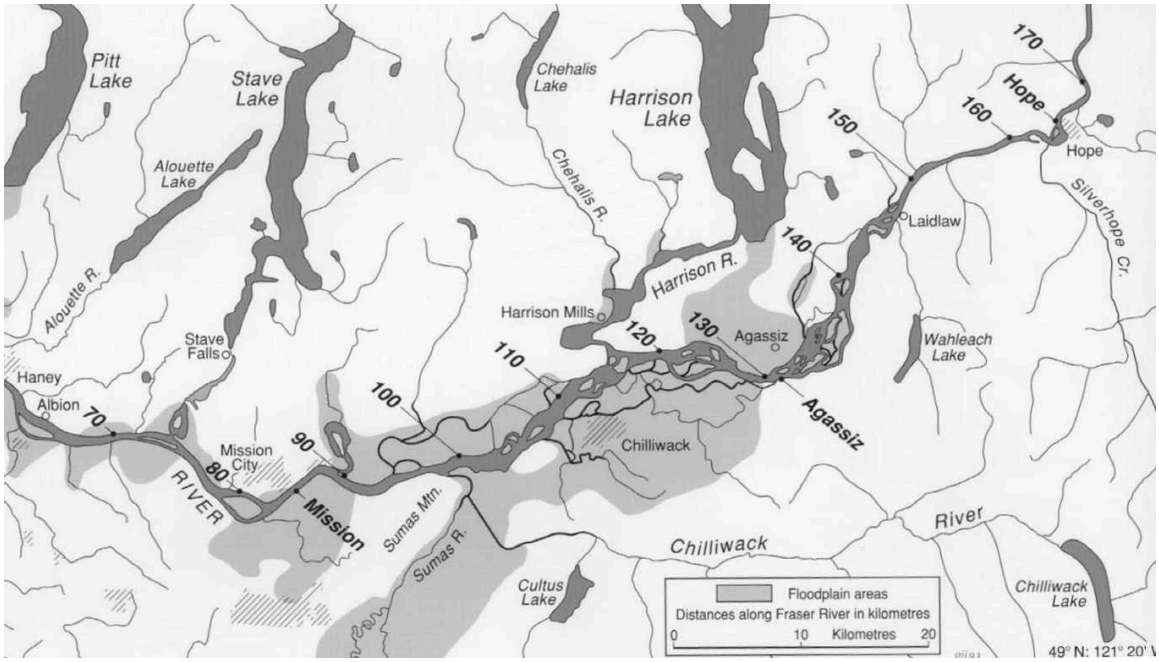

Figure 7: Lower Fraser River, depicting river kilometres and gauging stations (Church, Michael. Accessed 13 Aug. 2010. <http://www.geog.ubc.ca/fraserriver/largeimages/location.jpg>).

The Fraser River basin was glaciated in the Pleistocene, leaving thick glacial deposits in the basin and major tributaries. The rivers in this region have incised into these Quaternary sediments and supply the main sediment load from erosion of riverbanks and terraces (Church, 1990). Glacial till, glaciolacustrine silt, earthflow, and silty debris-flow deposits make up the bulk of the source material, which introduces mostly fine-grained (clay and silt) sediment. In addition, many lakes on principal tributaries intercept part of the sediment load. In comparison to many major river systems in the world the total sediment yield for the Fraser (~17 million tones/year) is not large (McLean et al., 1999).

2.2.1 Patterns of Sediment Transport at Agassiz

Agassiz gauging station is located between Laidlaw and Sumas Mountain, ~30 km upstream of Yaalstrick Bar. This section of the river consists of a "wandering" gravel-bed channel with many mid-channel islands and low-order braiding. At low water the channel exhibits prominent gravel bars and lateral bars that extend to the shore or islands, point bars are visible at bends, and mid-channel bars are located in areas of flow expansion (McLean et al., 1999).

Unstable bedforms exist in the channel including transient gravel "waves" which originate from upstream bank erosion or channel shifting from islands and banks. This eroded material migrates along the channel until it becomes incorporated into bars. The growth of the gravel bars changes flow conditions to produce higher shear stress at the adjacent banks, which in turn initiates new episodes of erosion and channel instability. The channel bed is composed of bimodal deposits with gravel as the coarse fraction (median in the range of 25-30 mm) and medium sand (0.3 mm) as the fine fraction. Sand-sized sediments generally account for less than 10% of the channel bed material at Agassiz. As such sand is carried as washload. The amount of silt and clay in washload at Agassiz is governed by the rate of sediment supply, and not by hydraulic conditions in the channel (McLean et al., 1999), while sand is governed by both. The suspended sediment load by grain-size is shown for Agassiz in Table 2-1.

Table 2-1: Suspended Sediment load for Agassiz by grain size (McLean et al., 1999).

Grain Size	Sediment Load (t yr^{-1})
Clay	$2.75x10^6$
Silt	$8.59x10^6$
Sand	$5.19x10^6$
Total	$16.5x10^6$

Seasonal variation in the suspended sediment load occurs at Agassiz and this pattern is seen in Figure 8. The supply of suspended sediment becomes depleted during the freshet, and flows between 7500 and 8000 m^3s^{-1}carry the largest proportion.

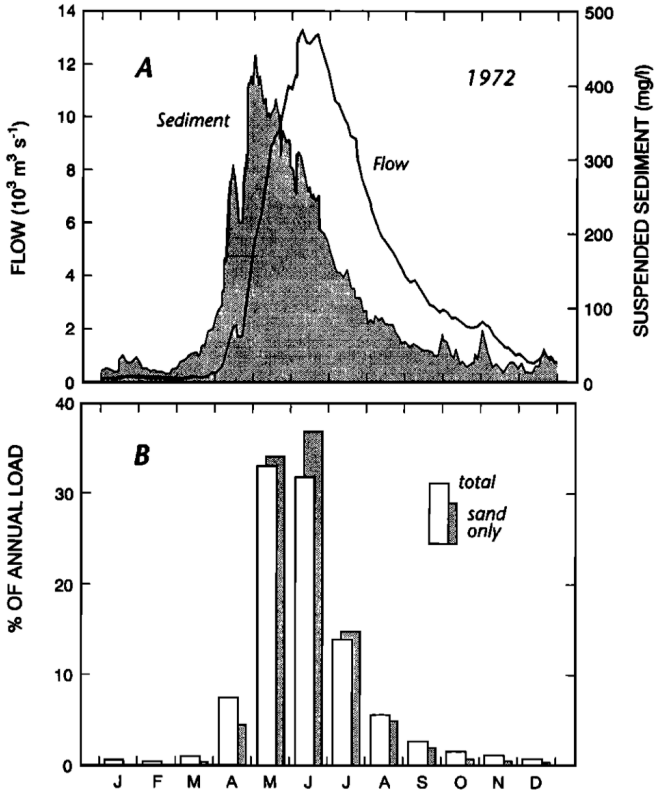

Figure 8: (A) Hydrographs of daily discharge and suspended-sediment concentration at Agassiz 1972 and (B) proportional distribution of average suspended load by month at Agassiz from 1966-1982 (Mclean et al., 1999).

The relationship between bed load transport rate and discharge is ill defined in the gravel-bedded reach of the Fraser near Agassiz. Considerable gravel transport begins at flows near 5000 m^3s^{-1}, which may be considered the threshold condition at which the armoured surface of the channel bed is mobilized. The transport rate of the gravel remains low throughout the entire range of flows experienced on the Fraser. Similar to the suspended load, the most significant bedload transport occurs at ~8000 m^3s^{-1}, where the bed shear stress is only ~50% greater than the nominal critical stress required to mobilize the armoured surface material. Lastly, most of the bed load movement occurs when transport is only weakly established in the "partial transport regime" of Wilcock and McArdell (1997) (McLean et al., 1999).

2.2.2 Patterns of Sediment Transport Near Mission

Near the town of Mission, BC, at Sumas Mountain, the river changes abruptly to a single thread sand-bedded channel and the sediment transport conditions change. Gravel-bed load is deposited upstream of Sumas Mountain. The wash load includes only very fine sand, silt, and clay and the bed load consists of medium and coarse sand. The sediment load by grain size is presented in Table 2-2. The medium and coarse sand loads are determined by the hydraulic channel conditions that govern entrainment rates from the bed rather than by the upstream sediment supply. Considerable variability is seen in bed load measurements at Mission (McLean et al., 1999).

Table 2-2: Suspended Sediment load for Mission by grain size (McLean et al., 1999).

Grain Size	Sediment Load (t yr^{-1})
Clay	$2.69x10^6$
Silt	$8.28x10^6$
Sand	$6.08x10^6$
Total	$17.1x10^6$

2.2.3 Location of Gravel-Sand Transition

Results presented by McLean et al. (1999) suggest that upstream of Yaalstrick Bar in the gravel-bedded reach, sand is being carried in suspension. At Mission, the bed is composed of sand across its width, which suggests that some of the suspended sand load from the gravel reach has been deposited. This lead McLean et al. (1999) to suggest that the gravel-sand transition should occur somewhere between Yaalstrick Bar and Mission.

Venditti et al. (2010c) re-examined the location of the gravel-sand transition using existing data by McLean et al. (1999) and datasets that have been collected since 2003. These include: (1) a low-resolution bed survey from 2003, (2) a high-resolution multibeam survey and Shipek bed material samples at high flow (~9800 m3s-1) in 2007, (3) dredge samples at low flow (~1000 m3s-1) in 2007 and 2008.They also examined river bed topography surveyed in the subsequent 2008 freshet. Their results are summarized in Figure 9 and Figure 10.

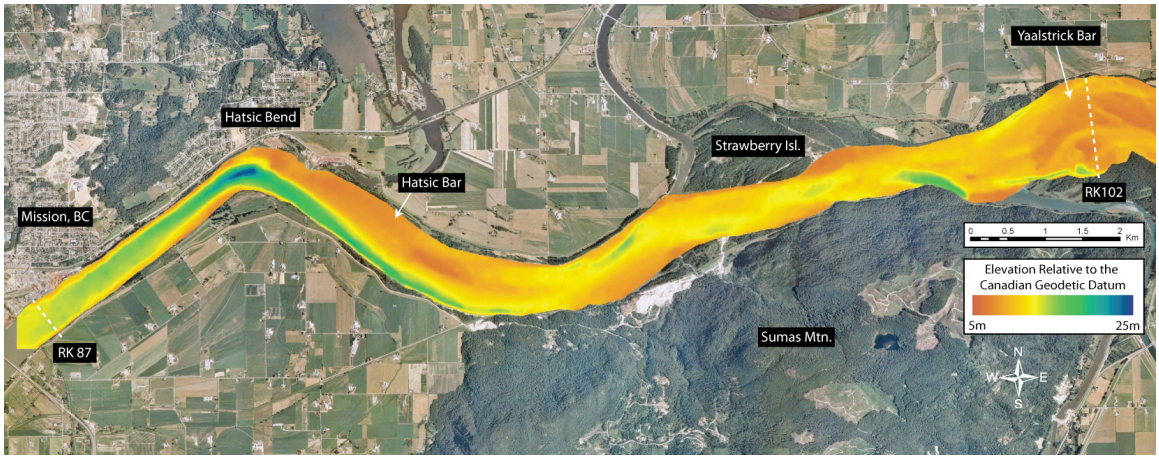

Figure 9: Bed topography in the gravel-sand transition reach observed during the 2008 freshet by Venditti et al. (2010c).

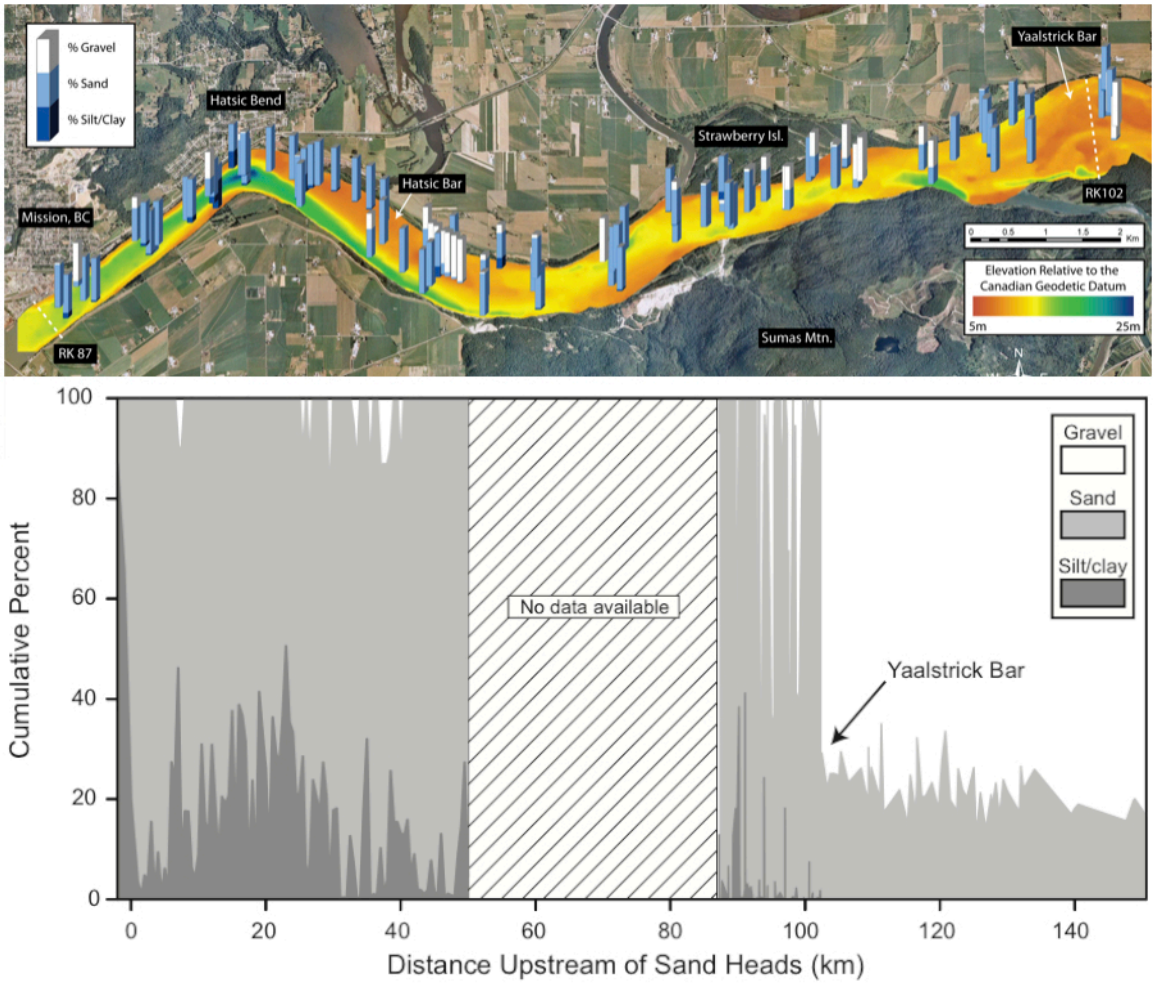

Figure 10: Gravel, sand and silt/clay distribution in the gravel-sand transition reach of the Fraser River (top panel) and downstream change in sediment size classes (bottom panel) (Venditti et al., 2010c).

Downstream of Yaalstrick Bar the riverbed topography displays multiple sub-aqueous channels and two major channels on either side of Yaalstrick Bar. A sinuous thalweg occurs between Sumas Mountain and Strawberry Island. In the first major bend downstream of Yaalstrick bar flow separation occurs and forms a large concave bank bench (*sensu* Hickin, 1979), Hatzic Bar. In this area the southern bank of the river is confined by bedrock and rip-rap, beyond Hatzic Bend the river is essentially unconfined, and the bed is deeply scoured (Ham, 2005). Between Yaalstrick Bar and Mission the Fraser becomes deeper and narrower.

There are strong spatial patterns in the bed surface grain size through the reach (Figure 10). Samples from Yaalstrick bar are gravel, but downstream the channel is almost entirely sand-bedded with gravel visible in deeply scoured pools and on bar heads that are immediately downstream of these pools. Hatzic Bar shows particularly strong along-bar fining, where the gravel head smoothly grades into sand on the bar surface. Between Yaalstrick Bar and Mission, the bed changes from ~70% gravel and ~30% sand to being entirely sand. Beyond Mission, the riverbed is composed of 0.3 mm sand until it reaches the Straight of Georgia (McLean et al., 1999).

Venditti et al. (2010c) interpret these patterns to indicate that the gravel-sand transition in the Fraser River is sharp and takes the form of an arrested gravel front. The patches of gravel downstream of Yaalstrick Bar suggest gravel is leaking downstream and being preferentially deposited in deeply scoured pools and on bar heads immediately downstream of the pools.

Flow and suspended sediment transport data is vital in advancing our knowledge of the processes occurring in the Fraser transition. Examining downstream gradients in suspended-sediment flux could aid in determining whether sand is coming out of suspension to form the sand-bedded reach near Mission, BC. Downstream gradients in shear stress would help understand the gravel mobility through this reach. This data was collected in the transition reach of the Fraser River and is discussed in detail in the following chapter.

3: METHODS

3.1 ADCP Observations

A four-beam 600 kHz Workhorse Rio Grand Acoustic Doppler Current Profiler (ADCP) manufactured by Teledyne RD Instruments (Figure 11) was used to collect velocity, depth and backscatter data. The ADCP was connected to a Trimble GPS Rover in real time kinematic (RTK) mode. The GPS rover obtained correction information from a base station located on a monumented survey marker.

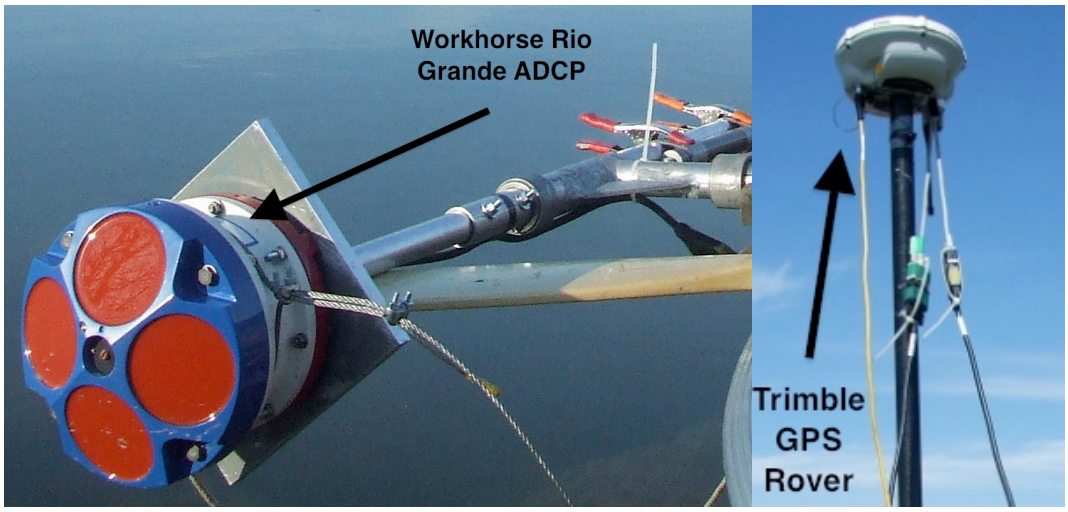

Figure 11: Workhorse Rio Grande ADCP mounted on a vessel and Trimble GPS rover.

3.1.1 ADCP Background and Specifications

The ADCP is based on the Doppler shift principle and measures the spatial averages of the 3 principal water velocity components in individual “bins” (depth cells) throughout a vertical column of water. The instrument transmits an acoustic pulse called a ping at a fixed frequency and ‘listens’ to echoes returning

from sound scatterers in the water. Sound scatterers are small particles or plankton that reflect the sound back to the ADCP. Scatterers are assumed to move at the same horizontal velocity as the water. When sound scatterers move away from the ADCP, the sound they perceive is Doppler-shifted to a lower frequency proportional to the relative velocity between the ADCP and scatterer. The backscattered acoustic energy is called echo intensity. As the ADCP transmits and receives sound, the Doppler shift is doubled. The change in the received frequency at the receiver (the Doppler shift) is calculated by:

$$F_d = 2F_S(V/C) \qquad (1)$$

where F_s is the frequency of the transmitted sound, V is the relative velocity between the source and receiver, and C is the speed of sound.

The ADCP calculates velocity relative to the ADCP. Velocity data have both speed and direction information. If the ADCP is within range of the bottom, it can obtain boat velocity from returns off the bottom. This is called bottom tracking. The bottom track information can be used to calculate the absolute velocity of the water. Bottom track information is only accurate when the bed is stationary. The ADCP obtains absolute direction information from an internal magnetic heading sensor.

A vessel-mounted ADCP uses multiple beams to obtain velocity in three dimensions and assumes that currents are uniform (homogeneous) across layers of constant depth. Multiple beams are pointed in different directions to sense different velocity components. Therefore, to measure three velocity components

(e.g. east, north, and up), there must be at least three acoustic beams. Figure 12 illustrates how the three velocity components are computed using the four acoustic beams of an ADCP. One pair of beams obtains one horizontal component and the vertical velocity component. The second pair of beams produces a second, perpendicular horizontal component as well as a second vertical velocity component. Thus, there are estimates of two horizontal velocity components and two estimates of the vertical velocity.

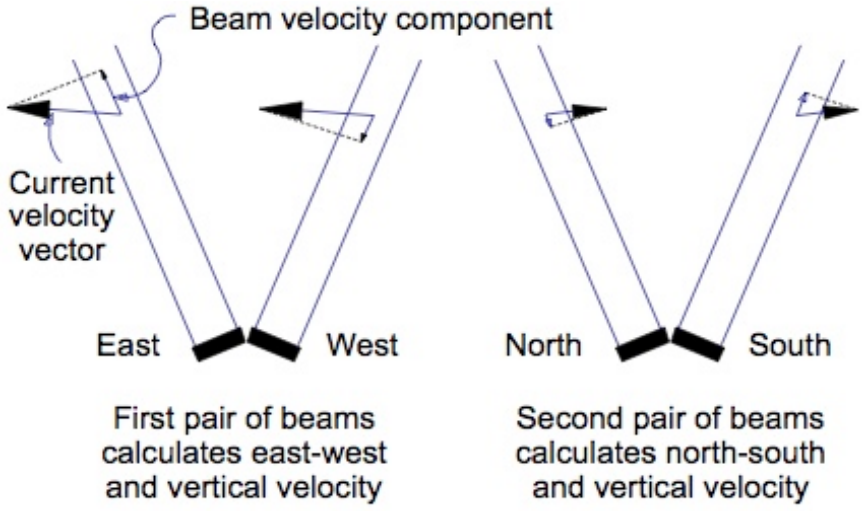

Figure 12: ADCP computing three velocity components using four acoustic beams; shows the relationship between beam and earth velocity components. The orientation is arbitrary (Teledyne RD Instruments, 2006).

Depth cells in an ADCP profile are always uniformly spaced and measure average velocity over the depth range of each depth cell. Averaging reduces the effects of spatial aliasing, which in a time series causes high frequency signals to look like low frequency signals. Averaging is not uniform over the depth cell range and depth cells are most sensitive to velocities at the centre of the cell and least sensitive at the edges (Figure 13). Adjacent bins are correlated because each bin employs Doppler backscatter from a triangularly weighted window with

a length equal to two bins causing neighbouring bins to obtain overlapping measurement volumes. Smoothing the observed velocity over the range of the depth cells rejects velocities with vertical variations smaller than a depth cell, and thus reduces measurement uncertainty. Regular spacing of velocity data over the profile makes it easier to process and interpret the measured data.

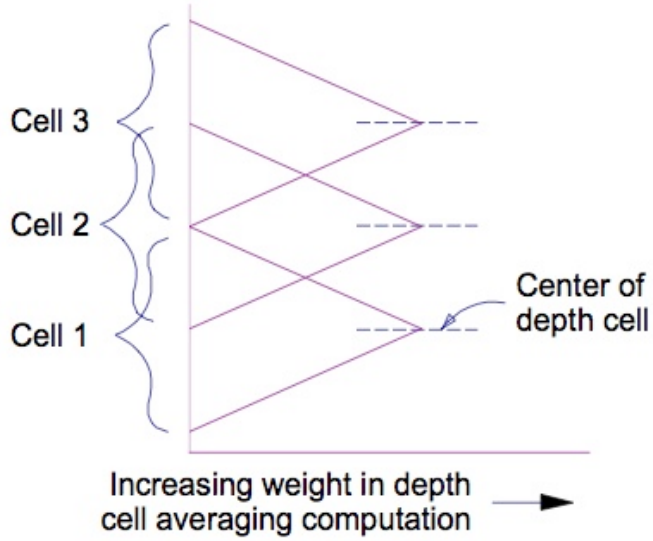

Figure 13: Triangular weight function: depth cells are more sensitive to currents at the centre of cells than at edges (Teledyne RD Instruments, 2006).

3.1.2 ADCP Field Data Collection

The goal of the ADCP data collection was to obtain a complete spatial representation of the flow and suspended-sediment transport concentrations in the gravel to sand transition zone of the Fraser River. Obtaining continuous spatial velocity and backscatter data would provide information on the gradients associated with the changes in sediment transport processes that control the location of the gravel-sand transition. As noted, this zone is located between Yaalstrick Bar and Mission Railway Bridge, where the data collection campaigns were based. ADCP data collection consisted of five field campaigns, which were

designed to represent five stages of the hydrograph and 'suspended sedigraph'. The five field campaigns and the 2009 water levels and discharges (>5000 m^3/s) are shown in Figure 14. In addition, the data were collected during the falling tide as most of the sediment transport occurs during those flows.

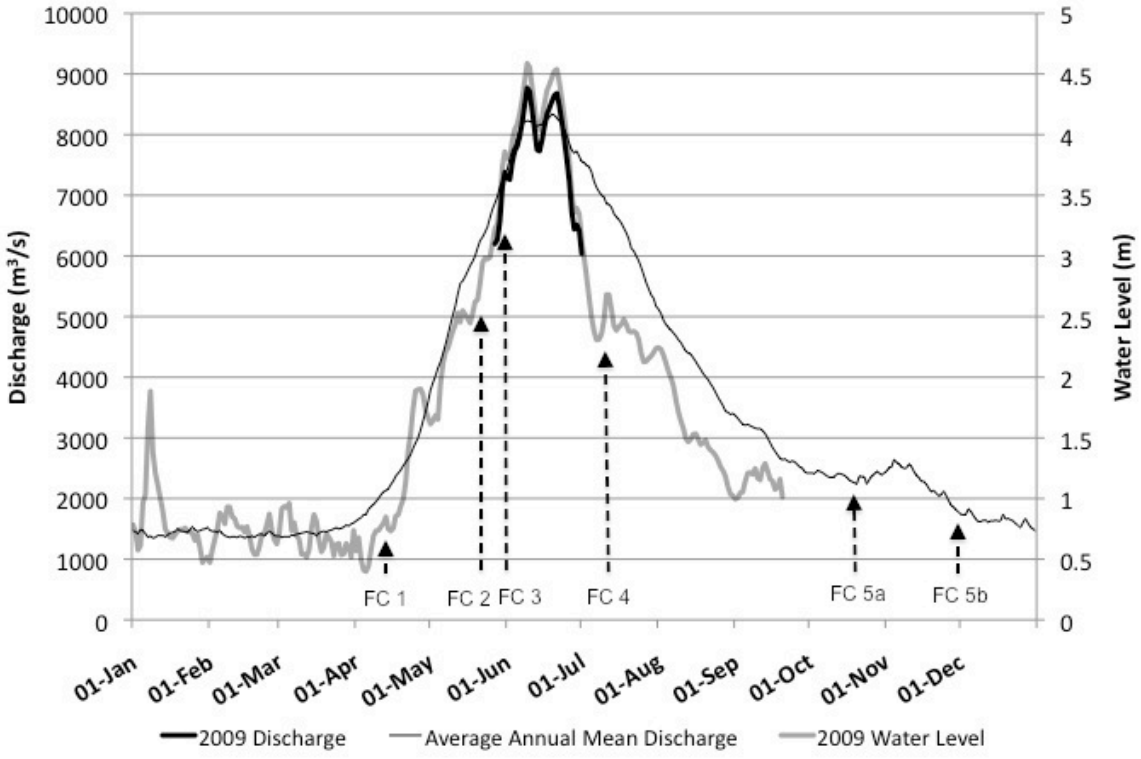

Figure 14: Dates of the field campaigns and 2009 hydrograph and water levels along with average annual hydrograph for Mission Station (data source: WSC).

The first data collection period occurred during low flows from April 8th 2009 to April 11th 2009 (FC 1). The second campaign occurred right before the freshet from May 21st 2009 to May 24th 2009 (FC 2). The third data collection period took place during the peak discharge from May 31st 2009 to June 3rd 2009 (FC 3). The fourth campaign occurred right after the peak discharge on July 9th and 10th 2009 (FC 4). Lastly, the final data collection period took place during low

flows on the falling limb of the hydrograph on October 18th 2009 (FC 5a) and December 1st 2009 (FC 5b). The last field collection was broken up due to illness and because falling tides occurred at night between October 18th and December 1st, during which it was unsafe to work on the river.

The ADCP and RTK GPS Rover were mounted on the side of a 4.9 m aluminium boat powered by a 30 hp outboard motor (Figure 15). This allowed the ADCP to stay submerged while the GPS obtained the location above the ADCP. Both instruments collected data in unison. An echosounder was also mounted on the boat but frequent instrument failures lead to a substandard record, so the data were not included in the analysis presented here. All depth measurements presented in this thesis were derived from an average of the 4 beams from the ADCP. Both the ADCP and GPS rover were connected to a laptop onboard and data were streamed and logged through WinRiver II (Teledyne RD Instruments, 2007).

Figure 15: Aluminium boat, which deployed ADCP, GPS rover, and echosounder.

The instruments collected data in two sections: from Mission to the Vancouver Sand and Gravel mine on Sumas Mountain and from the gravel mine to Yaalstrick Bar. This division can be seen in Figure 16 and is important because Geodetic Survey of Canada markers were available at either end of the gravel-sand transition reach. The GPS base station was placed on the markers and broadcasted signals to the roving GPS on the boat. Placing the base station on a marker whose location is known in space allows the GPS to be operated in real-time kinematic mode (RTK), reducing the vertical and horizontal GPS errors to tens of millimetres. The first survey marker (GCM 963918) was located at the Mission boat launch, which transmitted data to the gravel mine on Sumas Mountain. The second (GCM 453597) was located on McDonald Road roughly 14 river kilometres upstream. A location error was made with the Mission survey marker and is discussed in section 3.3.4 Mapping Spatial Distribution of Flow (pg. 48).

Figure 16: Data collection divided into Mission reach and McDonald reach.

During data collection the boat moved upstream from Mission, BC towards Nicomen Island, while traversing the river in a “zig-zag” pattern (Figure 17). This “zig-zag” pattern is optimal for this type of data collection as it ensures maximum continuity, greater spatial coverage, and reduces error when interpolating.

Figure 17: The “zig-zag” pattern used for field campaign 1 (April 8th 2009 – April 11th 2009) ADCP data collection.

3.2 LISST Observations

A Sequoia LISST-100X (laser *in-situ* scattering transmissometer) was used to measure suspended-sediment concentrations and particle size distributions for the purpose of calibrating ADCP backscatter to suspended-sediment concentration.

3.2.1 LISST Background and Specifications

The LISST-100X instrument (Figure 18) uses laser diffraction to obtain particle size-distributions. It consists of optics for producing a red 670 nm collimated laser beam, a specially constructed detector array, electronics for signal pre-amplification and processing, a data storage and scheduling computer, and a battery. The LISST-100X instrument obtains in-situ measurements of

grain-size distributions, optical transmission, particle volume concentration, depth, and temperature.

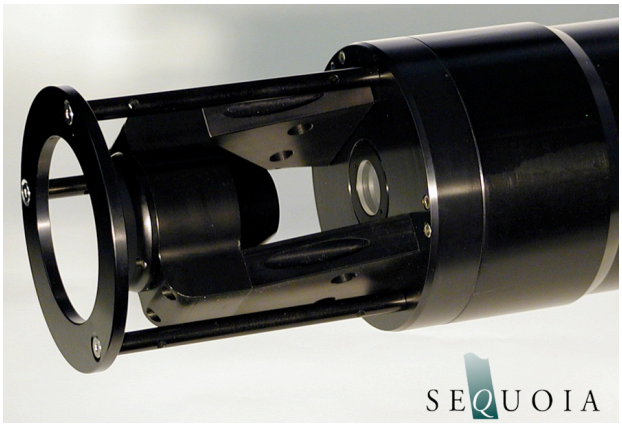

Figure 18: Laser *In-situ* Scattering Transmissometer (LISST) (Sequoia Scientific Inc., 2004).

The laser diffraction method for sizing particles determines grain-size distribution of an ensemble of particles, as opposed to counting type devices that size one particle at a time. When a collimated laser beam enters water, light is scattered by particles and sensed by a multi-ring detector behind a receiving lens, which senses particles at 32 specific log-spaced angle ranges (2.5-500 μm). A photodiode placed behind a centred opening measures optical transmission. This primary measurement is mathematically inverted to get the size distribution. The size distribution is presented as concentration (microlitres/litre) in each of 32 log-spaced size bins. The lower and upper limits and median sizes of the 32 bins are given in Table 3-1.

Table 3-1: Lower and upper bin limits, median bin sizes, and bins used in analysis for each of the 32 LISST size classes.

Bin	Lower bin limit (μm)	Upper bin limit (μm)	Median (μm)	Bins used for analysis
1	2.50	2.95	2.73	✗
2	2.95	3.48	3.22	✗
3	3.48	4.11	3.80	✗
4	4.11	4.85	4.48	✗
5	4.85	5.72	5.29	✓
6	5.72	6.75	6.24	✓
7	6.75	7.97	7.36	✓
8	7.97	9.40	8.69	✓
9	9.40	11.1	10.2	✓
10	11.1	13.1	12.1	✓
11	13.1	15.5	14.3	✓
12	15.5	18.2	16.8	✓
13	18.2	21.5	19.9	✓
14	21.5	25.4	23.5	✓
15	25.4	29.9	27.7	✓
16	30.0	35.3	32.7	✓
17	35.3	41.7	38.5	✓
18	41.7	49.2	45.5	✓
19	49.2	58.1	53.7	✓
20	58.1	68.5	63.3	✓
21	68.5	80.9	74.7	✓
22	80.9	95.4	88.2	✓
23	95.4	113	104	✓
24	113	133	128	✓
25	133	157	157	✓
26	157	185	186	✓
27	185	218	219	✓
28	218	258	259	✓
29	258	304	293	✓
30	304	359	332	✓
31	359	423	391	✗
32	423	500	462	✗

3.2.2 LISST Field Data Collection

LISST-100X was located in a drag-reducing metal cage and housing (Figure 19), and was deployed from a stern-mounted davit on an 11 metre gillnetter. Attempts were made to collect LISST data during all ADCP campaigns except campaign 4. However, successful deployments were only made during campaigns 1 and 3. Measurements during campaign 2 were compromised by a faulty path reduction module, that reduces the LISST measurement volume in high suspended-sediment concentrations. Measurements during campaign 5 were not completed due to illness.

Figure 19: LISST encased in sheet metal housing (left) and without sheet metal housing (right).

The boat was anchored at particular locations to collect vertical LISST profiles and measurements were collected at various depths. Each at-a-point sample was 5 minutes long and sampled at 1 Hz for 300 samples per point in a profile. The chosen locations were intended to obtain full spatial coverage, which

included profiles in the Mission reach, Hatzic reach, Sumas reach, and Yaalstrick reach (Figure 20).

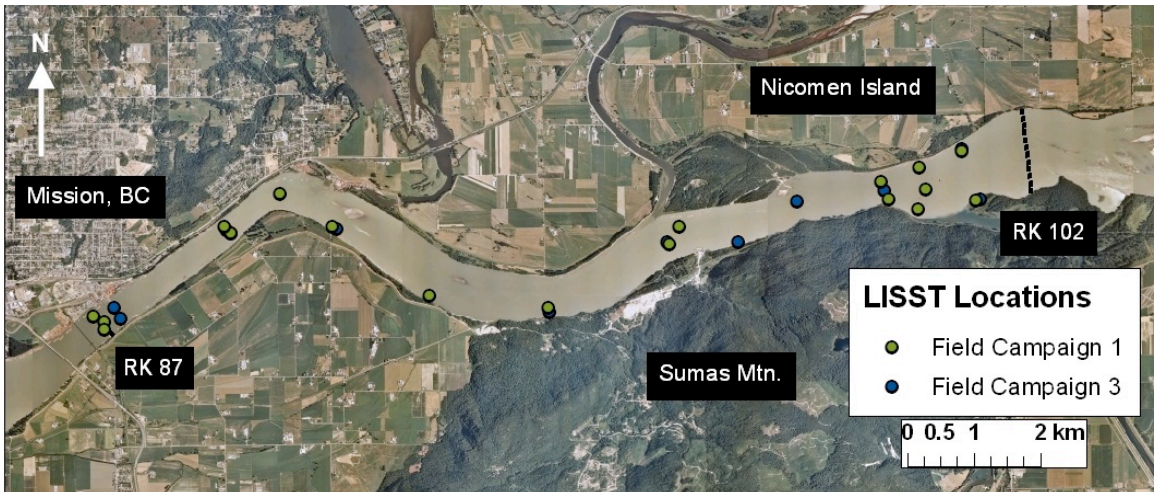

Figure 20: Locations of LISST profile data collection.

To correlate ADCP backscatter to LISST sediment concentrations, simultaneous LISST and ADCP measurements were required. As the instruments were mounted on separate vessels, the smaller aluminium boat had to be tethered to the larger anchored vessel and collect data in unison. During the two successful LISST field deployments a total of 17 simultaneous LISST and ADCP profiles were collected.

3.3 Data Analysis

3.3.1 ADCP Data

A software package developed by Colin Rennie (University of Ottawa) was used to extract all data and correct the data for magnetic variation, depth of the transducer head below water, and the height of the rover above the ADCP. This

package output all ADCP data in Matlab-file format, which was then used for further processing.

Depth, depth-averaged velocity, near-bed velocity, and shear stress were calculated from raw ADCP data. Depth (d) was obtained by averaging the depth of four beams. Depth-averaged velocity (U) was calculated from the bin velocities and averaged over the entire water column depth using:

$$U = \frac{\sum_{i=d}^{i=bed} u_i \times z_i}{d} \qquad (2)$$

where u_i is the velocity of bin i and z_i is the bin depth. In the calculation, the depth above and below the first and last measured bins was applied to the first and last measured bins, respectively.

Shear stress (τ) was estimated by first calculating shear velocity (u_*) using the same approach as Rennie and Church (2010). Shear velocity was estimated from the slope of a log fit to the entire measured streamwise velocity profile:

$$u = \frac{u_*}{\kappa}\ln(z) + \frac{u_*}{\kappa}\ln\left(\frac{30}{k_s}\right) \qquad (3)$$

where u is the velocity in the bin at height z above the mean bed elevation, κ is the von Kármán constant (0.41), and k_s is the bed roughness. Shear velocity was calculated from the slope of the line times κ. Then a known velocity at a known height was used to back calculate bed roughness, k_s. A moving average of 11

adjacent pings for each velocity profile was used when calculating *u*, because single ping velocity profiles are relatively noisy (Rennie and Church, 2010). To ensure that the velocity profile was sufficiently semilog-linear, shear velocity estimates were also weakly filtered if calculated k_s exceeded 5 m or was less than 0.1 mm (Rennie and Church, 2010). Shear stress (τ) was calculated from shear velocity using:

$$\tau = \rho u_*^2 \qquad (4)$$

where ρ is the density of water. Log-law shear velocity estimates based on depth-averaged or single velocity points may be more reliable than ones derived from the entire profile because the mean velocity reflects greater averaging of turbulent fluctuations and is less affected by near-bed errors (Sime et al., 2007). The method used in Sime et al. (2007) is not adopted here because it requires a priori estimates of k_s, which are difficult to obtain without local surface samples.

3.3.2 LISST Data

LISST data were analysed by first examining the optical transmission. Sequoia recommends a value of 70% for accurate grain-size measurements. Some flow campaigns had transmission values <70% due to high turbidity, which necessitated using a path reduction module that reduced the measurement volume by 90%.

The second step in the LISST data analysis was to plot the particle size distributions as a probability distribution function (PDF) and a cumulative

distribution function (CDF). As every sample contained roughly three hundred pings, separate CDF and PDF graphs were made for each sample.

In addition, for every sample, the mean concentration, mean pressure (depth below water surface), cumulative concentration, and percent finer were calculated. Arithmetic mean, D_a, and arithmetic standard deviation, σ_a, were calculated using:

$$D_a = \frac{\sum\left(f_i D_i\right)}{\sum f_i} \tag{5}$$

$$\sigma_a = \frac{\sum f_i\left(D_i - D_a\right)^2}{\sum f_i} \tag{6}$$

where f_i is the fraction of a particular size D_i. Geometric mean, D_g, and geometric standard deviation, σ_g, were calculated using:

$$D_g = \exp\left(\frac{\sum\left(f_i \ln D_i\right)}{\sum f_i}\right) \tag{7}$$

$$\sigma_g = \exp\left(\frac{\sum f_i\left(\ln D_i - \ln D_a\right)^2}{\sum f_i}\right) \tag{8}$$

Grain-size percentiles were obtained by the interpolation of the grain size distribution in Matlab using Piecewise Cubic Hermite interpolation of the CDF.

The PDF curves for each sample were reviewed to detect erroneous data. They indicated that the data collected during the second field campaign were flawed and therefore unusable in this analysis. This occurred because sediment

collected between the optics window in the installed PRM which caused the LISST to measure the trapped particles along with the particles in the passing water. This was not a problem in later deployments as a new PRM was installed. In addition, the PDF plots indicated a spike in the first 4 and last 2 grain-size classes. This is common and occurs because these grain-size bins are at the edge of the laser detector. If the laser alignment is not perfect these bins are susceptible to large errors (Sequoia Scientific, Personal Communication, 2009). These grain-size classes were removed in all further calculations and plotting. The grain-size range changed from 2.5-500 µm to 4.85-358.57 µm (lower to upper limit of bottom and top bin). This modification and can be seen in Figure 21 and Table 3-1. All parameters were then recalculated.

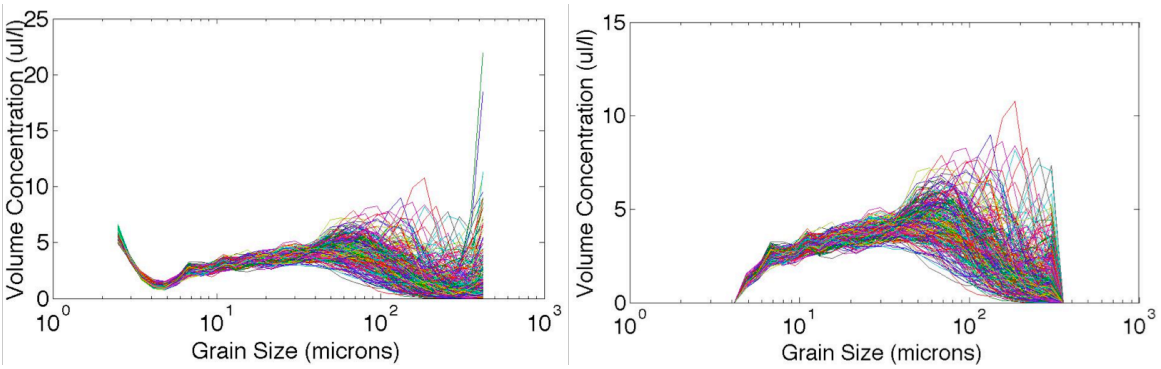

Figure 21: Cleaning data by removing first 4 and last 2 grain-size classes. Left graph shows all 32 classes while right graph shows cleaned data.

3.3.3 ADCP Backscatter Calibration Against LISST Data

3.3.3.1 Background

To understand the sediment transport processes in the gravel-sand transition of the Fraser River it was important to obtain a continuous spatial representation of concentration of suspended solids (SSC). The traditional

method for obtaining SSC measurements is bottle sampling and subsequent analysis. The method is time consuming and labour intensive. The results are limited to the sampling locations. Obtaining enough bottle samples to satisfy the need for spatially resolved observations required here was simply not possible. Field instruments such as optical backscatterance sensors (OBS) and transmissometers (LISST) can be used to obtain observations more rapidly. However, these instruments collect data at a point and obtaining many data points is logistically difficult. Therefore, these instruments cannot provide the spatial representation required for this research. As the use of ADCPs to measure velocities has become more common, it has been shown that echo intensity (EI), a measure of signal strength of the echo returning from the ADCP's transmit pulse, is correlated with and can be used to estimate suspend-sediment concentrations in a wide range of conditions (e.g., Thorne et al., 1990; Thevenot et al., 1992; Reichel and Nachtnebel, 1994; Deines, 1999; Gartner, 2004; Topping et al., 2004; Kostaschuk et al., 2005; Wall et al., 2006; Topping et al., 2007;). Here the approach by Wright et al. (2010) is used to obtain a spatially resolved estimate of SSC.

The process of converting echo intensity to sediment concentrations is multifaceted and factors such as complex transmission losses from beam spreading and attenuation need to be considered. Echo intensity depends on environmental characteristics such as suspended material, salinity, temperature, and pressure, and instrument characteristics such as power, transducer size, and frequency (Gartner, 2004). Echo intensity is corrected and normalized to account

for the factors mentioned above to calculate Acoustic Backscatter (ABS), which can be linked to SSC. This relation is based on a formula, which was derived from the sonar equation for sound scattering from small particles (Gartner, 2004). The equation in exponential form is:

$$SSC_{(est)} = 10^{(A+B*ABS)} \quad (9)$$

The exponent contains a term for the acoustic backscatter, ABS, and terms for an intercept, A, and slope, B, determined by regression of simultaneous measurements of ABS and mass concentration (SSC_{meas}) on a semi-log plot in the form of $\log(SSC_{meas})=A+B*ABS$ (Gartner, 2004).

The final correlation is dependent on the field conditions and environmental characteristics. A theoretical solution to equation 9 is not possible, so each ADCP must be calibrated *in situ*. This was accomplished by correlating a number of measures of ABS to concentrations measured using the LISST.

3.3.3.2 Converting Echo Intensity to Water and Sediment Corrected Backscatter

The ADCP records echo intensity in counts and this raw backscatter value is converted to measured backscatter, *MB*, in decibels. This was done by multiplying EI values by an instrument-specific and beam-specific scale factor, which was available from RD Instruments by request (RD Instruments, Personal communication, 2009; Table 3-2). In this analysis only beam three was used because it was the forward facing beam.

Table 3-2: Scale factors used to convert echo intensity counts to measured backscatter in decibels

Beam	Scale Factor
1	0.3922
2	0.3943
3	0.3979
4	0.3911

The absorption along the beam due to water, α_w, needs to be accounted for. It was computed from the relation of Schulkin and Marsh (1962), assuming zero salinity and pressure:

$$\alpha_w = 8.686 \cdot 3.38 \times 10^{-6} \frac{f^2}{f_T} \qquad (10)$$

where

$$f_T = 21.9 \times 10^{[6-1520/(T+273)]} \qquad (11)$$

Where f_T is frequency of the ADCP in kHz and T is water temperature in °C. Beam spreading losses (function of range only) and water absorption losses were then used to compute the water-corrected backscatter for each measured velocity bin

$$WCB = MB + 20\log_{10} R + 2\alpha_w R \qquad (12)$$

where R is the distance along the beam to each cell.

Sediment attenuation acts similarly to the water absorption as it is also a two-way loss along the beam range, R. Assuming that the remaining slope of the

WCB profile was primarily due to sediment attenuation, the sediment attenuation coefficient, α_s, was computed as follows:

$$\alpha_s = -\frac{1}{2}\overline{\frac{d}{dR}(WCB)} \tag{13}$$

where $\overline{\frac{d}{dR}(WCB)}$ denotes the slope of the least-squares linear regression between WCB and R. The -1/2 multiplier accounts for the two-way losses. This results in an attenuation coefficient in dB/m. The profile was then corrected for attenuation due to sediment, which produces the sediment-corrected backscatter:

$$SCB = WCB + 2\alpha_s R \tag{14}$$

The relations were then attempted between these measures of acoustic backscatter and LISST derived SSC (presented in the Results section).

3.3.3.3 Limitations When Using ADCP as Surrogate for SSC

There are a few limitations when using an ADCP as a surrogate for suspended-sediment concentration. First, as ADCPs are single-frequency instruments, they are unable to recognize if changes in EI are associated with changes in sediment concentration or changes in particle-size distribution (Reichel and Nachtnebel, 1994). If there is a change in grain size the instrument interprets an increase in concentration. Therefore, interpreting EI data requires additional information about the scattering particles. Second, the error in SSC increases as the ratio of particle circumference to acoustic wavelength approaches 1 (Gartner, 2004). A third limitation is that ADCPs are meant to

detect acoustic frequency changes in current profiles and less accurately measure amplitude changes related to EI measurements (Schaafsma et al., 1997).

Other factors that make the relationship between EI and SSC complex include the challenges associated with collecting simultaneous data from a surrogate (OBS, LISST) or water sample and an ADCP, the need for correcting data to account for the loss of acoustic energy with distance from ADCP (attenuation corrections), and lastly, normalizations for fixed and dynamic differences between instruments and instrument components over time (Wall et al., 2006). The last two were not problems for this deployment.

3.3.4 Mapping Spatial Distribution of Flow

Maps of the spatial distribution of flow consisted of five attributes for the five ADCP field campaigns; these include: (1) depth, (2) depth averaged velocity (magnitude and direction), (3) shear stress, (4) SSC derived from WCB and (5) suspended sediment flux. All data were exported as ASCII files from Matlab into ArcMap 9.3 and projected into Universal Transverse Mercator (UTM) coordinates with the WGS84 datum. Aerial photographs taken in 1995 by Selkirk Remote Sensing at 1 metre resolution for this region were provided by Michael Church (UBC).

Several modifications were made to the data set to yield accurate maps from the processed data. First, both depth-averaged and near-bed north and east velocities were converted to magnitude and direction. The second

modification only pertained to the data collected using the Mission benchmark. After data collection concluded, it was realised that the survey marker location used for the RTK-GPS base station location in the field was incorrect. The location of GCM 963918 was input to the RTK-GPS software, but the base station was located over GCM 635201. As the two survey markers were in a close proximity to one another, this correction consisted of adding or subtracting the difference to the sample locations (Table 3-3).

Table 3-3: The difference between the benchmark used for data collection (GCM 963918) and the correct benchmark (GCM 635201).

	GCM 963918	GCM 635201	Difference
Northing	5441930 mN	5441953.367 mN	+23.367 m
Easting	550970 mE	550879.794 mE	-90..206 m
Elevation	6.695 m	8.324 m	+1.692 m

Because of unpredictable field conditions and limited time frame for field data collection the GPS data quality was not always RTK quality. This was due to poor satellite coverage during some time periods. RTK-GPS requires a minimum of five satellites to operate. This issue affected data that were direction dependent such as depth-averaged and near-bed velocity directions. Field campaigns 3-5 were most influenced.

Many different interpolations were tested to determine which one provided meaningful continuous maps of the gravel-sand transition reach. Rennie and Church (2010) created maps of depth-averaged water velocity, shear velocity, and apparent bed load velocity using kriging. Kriging is an advanced

geostatistical procedure that generates an estimated surface from a scattered set of x-y coordinates with z-values. Kriging is based on the regionalized variable theory that assumes that the spatial variation in the phenomenon represented by the z-values is statistically homogeneous throughout the surface. In ArcMap 9.3 kriging involves an interactive investigation of the spatial behaviour of the phenomenon represented by the z-values before selecting the best estimation method for generating the output surface. In this study, many different kriging estimation methods were applied to the data but all generated results that portrayed the flow parameters unrealistically and thus proved to be a poor interpolation technique for this data set.

The interpolation technique that portrayed the patterns in the raw data most realistically was natural neighbour interpolation. Natural neighbour interpolation finds the closest subset of input samples to a query point and applies weights to them based on proportionate areas in order to interpolate a value (Sibson, 1981). This method is local, using only a subset of samples that surround a query point, and interpolated z-values are within the range of the samples used. Natural neighbour interpolation does not infer trends and does not produce peaks, pits, ridges or valleys that are not already represented by the input samples. The surface passes through the input samples and is smooth everywhere except at locations of the input samples. It adapts locally to the structure of the input data, and requires no input from the user pertaining to search radius, sample count, or shape. It works equally well with regularly and irregularly distributed data (Watson, 1992). The natural neighbour interpolation

technique in ArcMap 9.3 was optimal as it was able to efficiently handle the number of sample points in this analysis and create a realistic continuous map of the raw data. The difference between kriging and natural neighbour interpolations is shown in Figure 22.

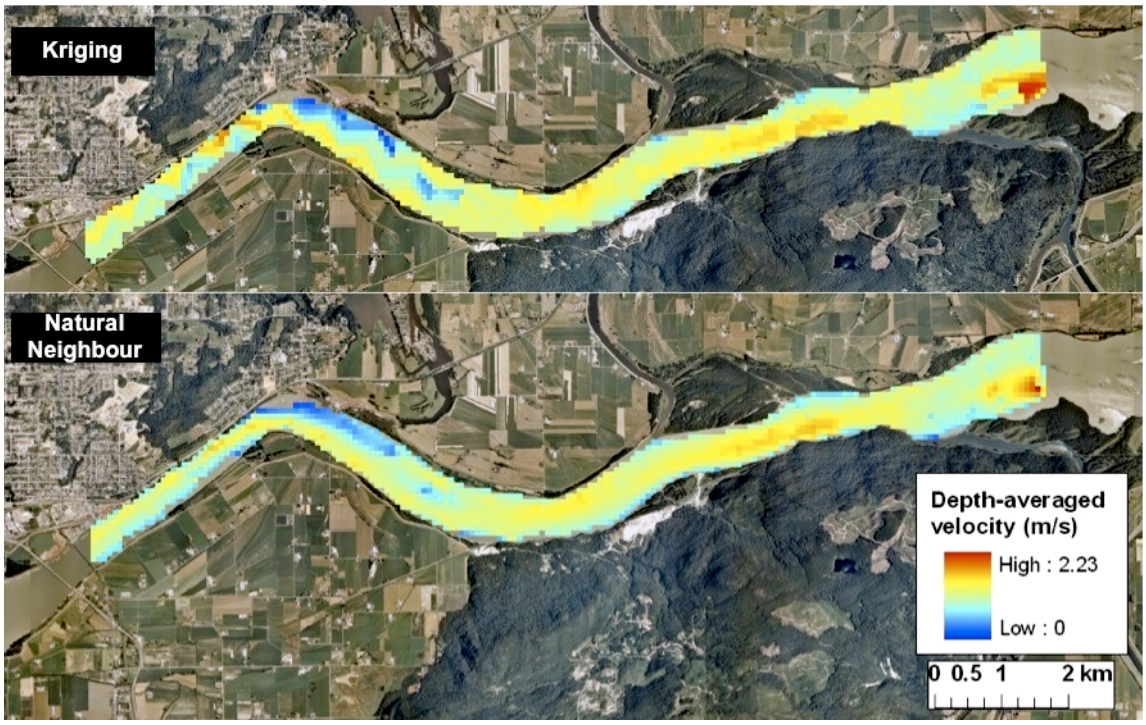

Figure 22: Difference between kriging and natural neighbour interpolations.

4: RESULTS

4.1 Backscatter and Suspended-Sediment Concentration Calibration

Six calibration methods were tested to produce a meaningful correlation between backscatter and SSC, to model SSC in the gravel-sand transition reach of the Fraser River. All calibration methods were attempted using time-averaged ADCP and LISST data. A summary of the calibration methods is presented in Table 4-1.

Table 4-1: Summary of ADCP LISST correlation techniques.

Method	Independent Variable	Dependent Variable	R^2	p-value	Figure
1	WCB	Log10 total SSC	0.81	1.45×10^{-47}	23
2	SCB	Log10 total SSC	0.61	3.01×10^{-28}	24
3	Sediment Attenuation	Silt-clay concentration	0.27	3.26×10^{-2}	25
4	SCB	Log10 sand concentration	0.56	5.58×10^{-4}	26
5	WCB	Log10 total SSC	0.85	1.75×10^{-7}	27
6	SCB	Log10 total SSC	0.67	5.45×10^{-5}	28

4.1.1 Point Measurement Correlations

The first approach was to correlate the WCB and SCB with each LISST sample. This method required locating the backscatter sample for the same depth as the LISST sample. This method is considered ideal because it yields a larger number of sample points (130 points) for the correlation than if the data were depth-averaged. The results can be seen in Figure 23 and Figure 24, respectively. The relation between both WCB and SCB, and SSC are statistically

significant at the 99% confidence interval. WCB explains 81% of the variability in SSC, and SCB explains 61% of the variability in SSC.

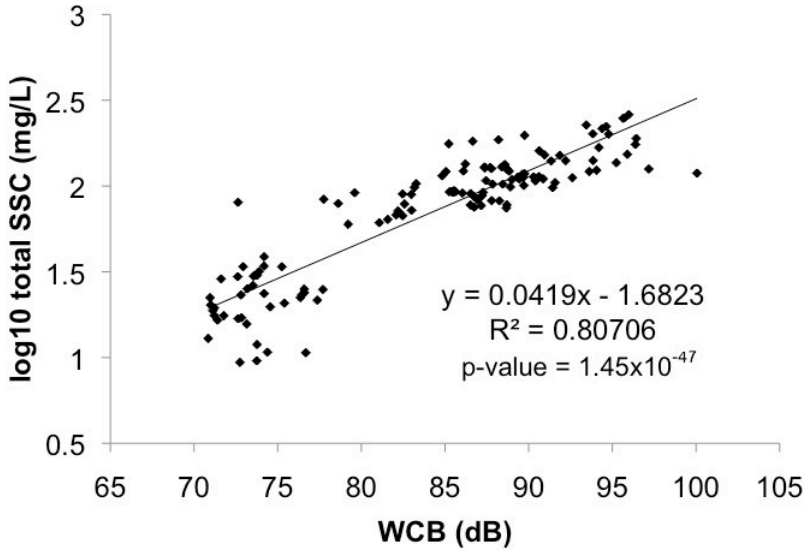

Figure 23: Bin by bin correlation between log10 SSC and WCB (dB).

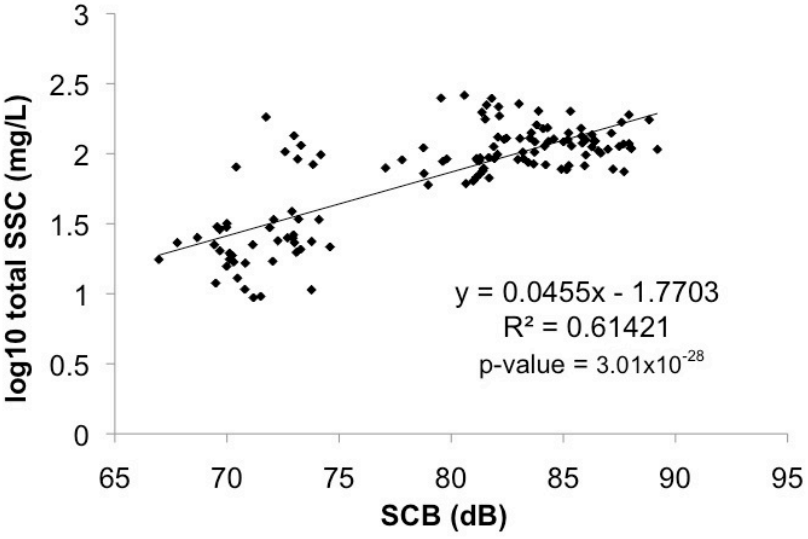

Figure 24: Bin by bin correlation between log10 SSC and SCB (dB).

4.1.2 Grain Size Specific Correlations

Wright et al., (2010), suggest that the sediment attenuation coefficient for rivers is primarily controlled by fines (i.e. silt and clay-sized particles) and that

backscatter (i.e. *SCB*) is primarily controlled by sand-sized particles. Attenuation is much greater for clay than sand, while backscatter is much greater for sand than clay (Wright et al., 2010). This method was attempted and the sediment attenuation coefficient was correlated against the depth-averaged silt and clay (<63 microns) LISST concentrations (Figure 25). Depth-averaged sediment corrected backscatter was correlated against the depth-averaged log10 sand (>63 microns) LISST concentrations (Figure 26). The relation between sediment attenuation and suspended silt-clay concentrations, and SCB and suspended sand concentrations are statistically significant at the 99% confidence interval. Sediment attenuation explains 27% of the variability in suspended silt-clay concentrations, and SCB explains 56% of the variability in suspended sand concentrations. Although the relation in Figure 25 is significant it is not known why the data are clustered as shown.

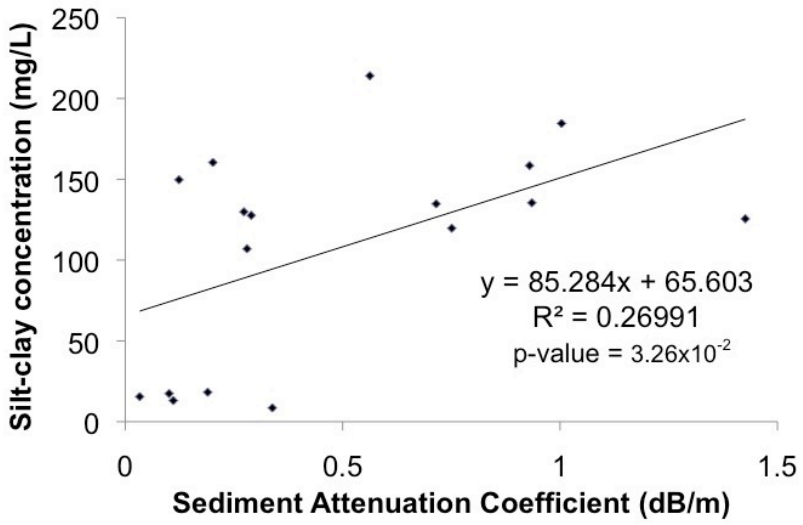

Figure 25: Correlation between sediment attenuation coefficient (dB/m) and depth-averaged silt-clay concentration (mg/L).

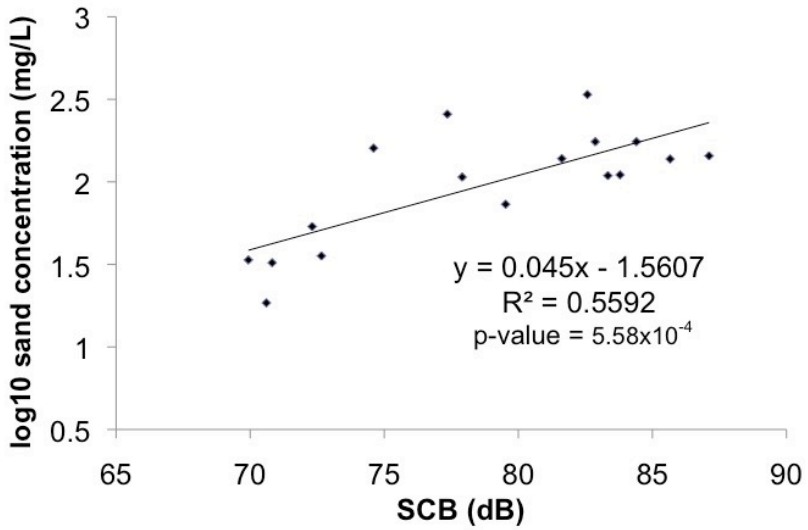

Figure 26: Correlation between depth-averaged sediment corrected backscatter (dB) and depth-averaged log10 sand concentrations.

According to Wright et al. (2010), the sediment attenuation and depth-averaged silt-clay concentration calibration (Figure 25) should be roughly linear and the SCB and sand calibration (Figure 26) should be roughly log-linear. It is clear, however, that the correlation between these variables is weak, especially for silt-clay and sediment attenuation. When comparing silt-clay concentrations and attenuation values to the analysis by Wright et al. (2010), it was evident that the silt-clay concentrations were too low for attenuation. Therefore, separating the concentrations into grain-size classes was not pursued further. One of the reasons this may have occurred is that grain size was changing along the beam. This violates one of the assumptions of this type of analysis.

4.1.3 Depth-Averaged Correlations

One way to avoid the complications associated with changes in grain size with depth is to avoid a bin-by-bin correlation and grain-size separation by using beam integrated measures of backscatter.

Two sets of graphs were produced using depth-averaged SSC, WCB, and SCB data correlating WCB and log10 total concentration (Figure 27), and SCB and log10 total concentration (Figure 28). Although this method reduced the data set to 17 samples, the relation between both WCB and SCB, and SSC are statistically significant at the 99% confidence interval. WCB explains 85% of the variability in SSC, and SCB explains 67% of the variability in SSC.

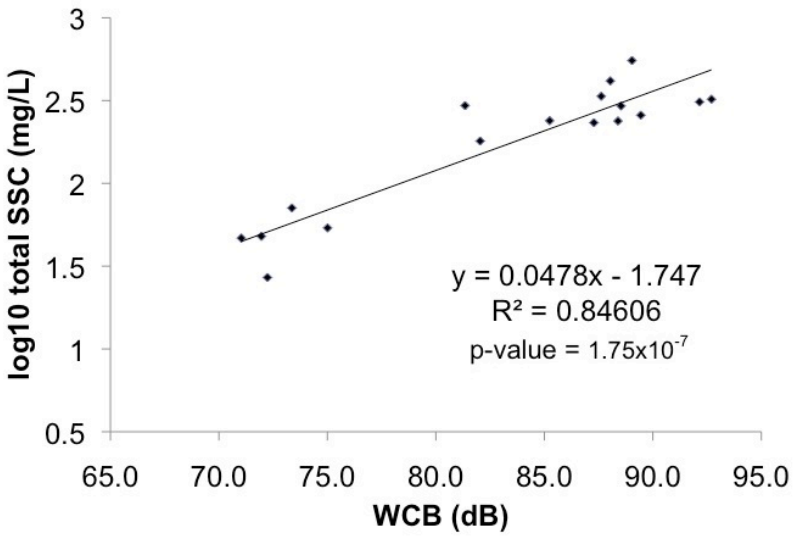

Figure 27: Correlation between depth-averaged WCB (dB) and depth-averaged total SSC.

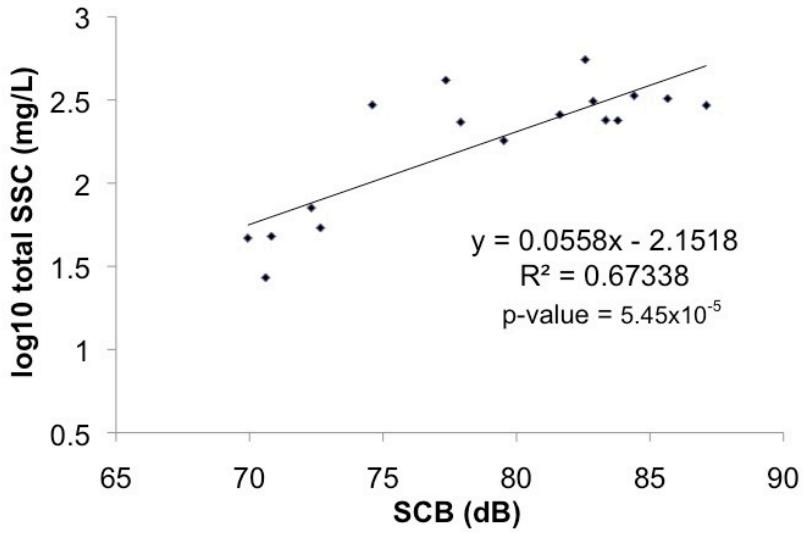

Figure 28: Correlation between depth-averaged SCB (dB) and depth-averaged total SSC.

Although all methods produced statistically significant results, the depth-averaged WCB and depth-averaged total SSC were used for the calibration. Bin-by-bin correlations were not chosen for the calibration because grain size changes along the beam complicated the signal. Grain size specific correlations were also dismissed because silt-clay concentrations were too low for sediment attenuation. The depth-averaged correlations reduced error, had the highest correlations, avoided complications associated with changes in grain size with depth, and produced physically meaningful results.

4.2 Fluid Flow Through the Gravel-Sand Transition

Fluid flow through the gravel-sand transition reach is illustrated by three flow parameters: depth; depth-averaged velocity; and shear stress. Downstream gradients in these parameters can aid in determining whether sand from the gravel reach is coming out of suspension in the sand-bedded reach and can aid

in determining what size sediment is in motion during low and high flows. Figures 29 to 31 illustrate flow parameter maps from each field campaign and for the entire gravel-sand transition reach at 80-metre resolution. Descriptive statistics (Figures 32 to 34) show the minimum, maximum, mean, and standard deviation for each of the fluid flow maps for each field campaign.

River topography (Figure 29) has not changed significantly since the work of Venditti et al., (2010c). Yaalstrick Bar continues to narrow downstream, with two channels on either side. A sinuous thalweg is visible downstream of Yaalstrick Bar towards Sumas Mountain. The river becomes deeper and narrower downstream. During high flows, these patterns are exaggerated as the depth increases. The mean depth was the highest during the third field campaign (8.89 m) (Figure 32).

Depth-averaged velocity (Figure 30) is highest in the channel south of Yaalstrick Bar. This high velocity core shifts from the south bank at low flows to over the bar at high flows. This occurs because at low stage the flow is constrained, and at high stage the channel gets wider allowing flow over the bar. Higher velocities seem to follow the sinuous thalweg and are also observed on the south bank at Sumas Mountain along the bedrock bank. Shoaling onto Hatzic Bar can be seen at high flows, which is how the bar is formed and maintained. Downstream of Hatzic bend along the north bank higher velocity is also observed at all flows. Field campaign 3 had the highest maximum and average depth-averaged velocities at 2.23 m/s and 1.09 m/s, respectively. The highest standard deviation was observed during FC 4 (0.31 m/s) and the second highest during

FC 3 (0.27 m/s), while the lowest was observed during the first field campaign (0.19 m/s) (Figure 33).

Shear stress maps (Figure 31) follow a similar pattern to depth-averaged velocity maps. During low flows it is evident that higher shear stress values exist at the upstream (east) end of the transition near Yaalstrick Bar. However, during high flows, especially during the third field campaign, it is clear that a declining downstream pattern does not exist. More specifically, high shear stress values are located in areas of confinement such as right before Hatzic bend, south of Hatzic Bar. Shear stress is low over Hatzic Bar in the higher flow campaigns. Lastly, a shear stress reversal is seen at Yaalstrick Bar. At low flows high shear stress is observed in the south channel. However, during high flows Yaalstrick Bar experiences high shear stress while low shear stress is exerted in the channel. During the first field campaign high shear stress is evident just downstream of the inflow of Dewdney Slough, but this is due to anomalous velocities measured by the ADCP. The highest mean shear stress was observed during the third field campaign while the lowest was observed during the first (10.08 N/m^2 and 1.57 N/m^2, respectively). The highest standard deviation was observed during the second field campaign (5.95 N/m^2) and similar standard deviations were observed during the third and fourth field campaigns (5.06 N/m^2 and 5.08 N/m^2, respectively) (Figure 34).

Shear stress was calculated for the Mission and Sumas reaches from the depth-slope product for a comparison of mapped values and to examine if a change is observed downstream (Table 4-2). Although the values are slightly

lower, they are similar. The decline downstream is not significant which also indicates that the results presented here are reasonable.

Table 4-2: Comparison of map shear stress and depth-slope product shear stress for the Mission and Sumas reaches.

Reach	Shear Stress (N/m^2)	Map Shear Stress (N/m^2)
Mission	6.04	10.07
Sumas	6.75	10.08

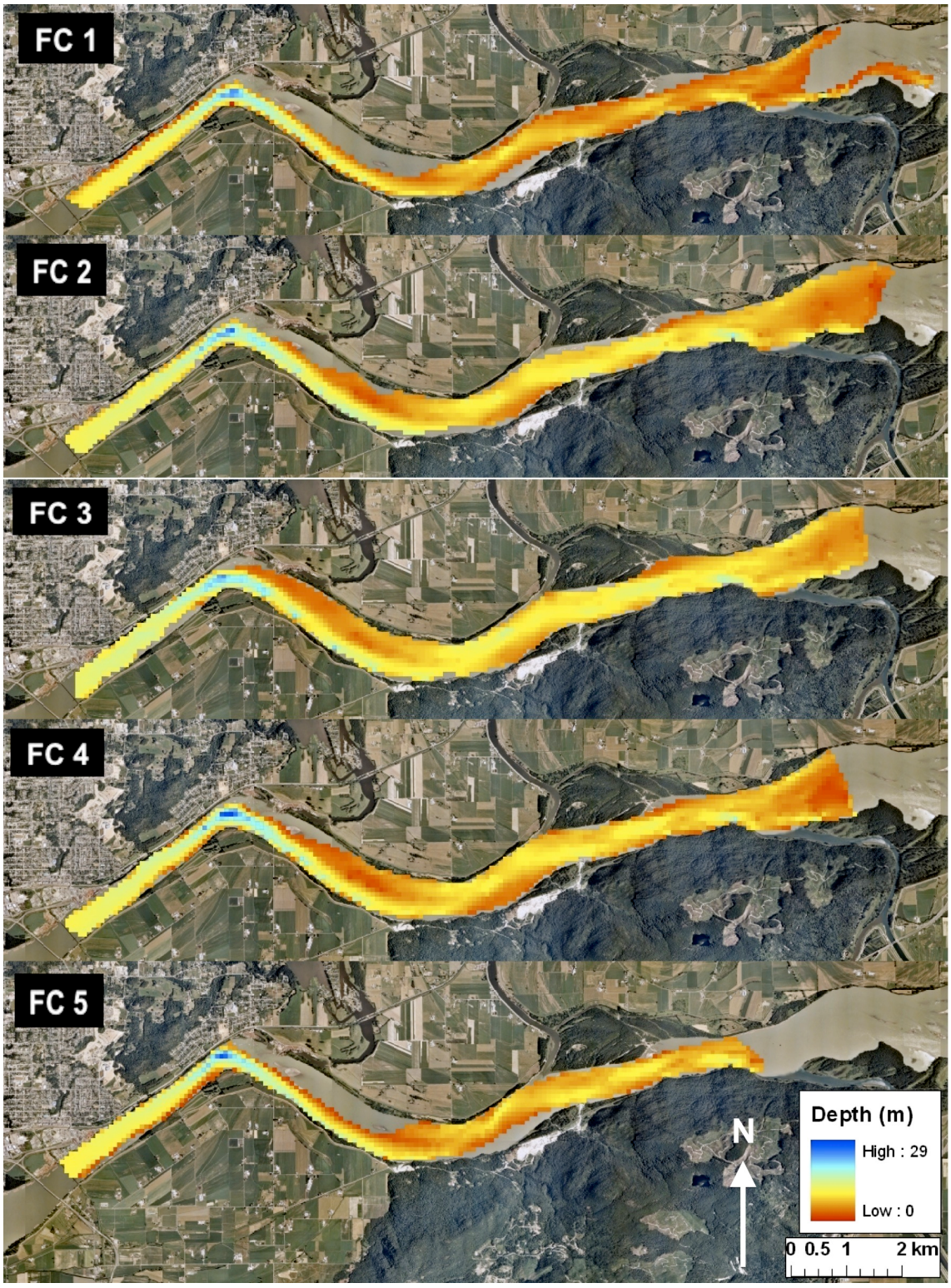

Figure 29: Spatial representation of depth for all field campaigns in 80-m resolution.

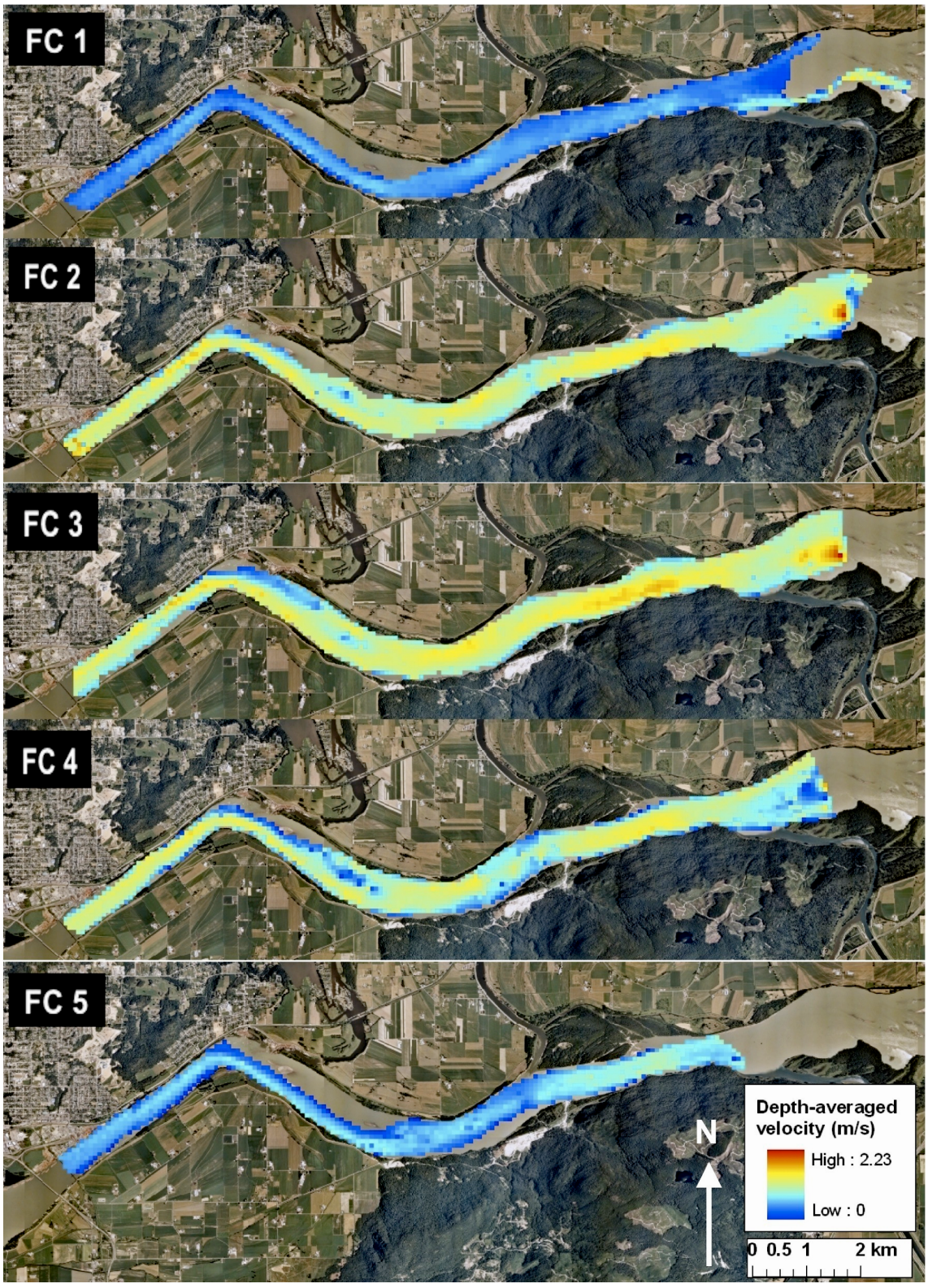

Figure 30: Spatial representation of depth-averaged velocity for all field campaigns in 80-m resolution.

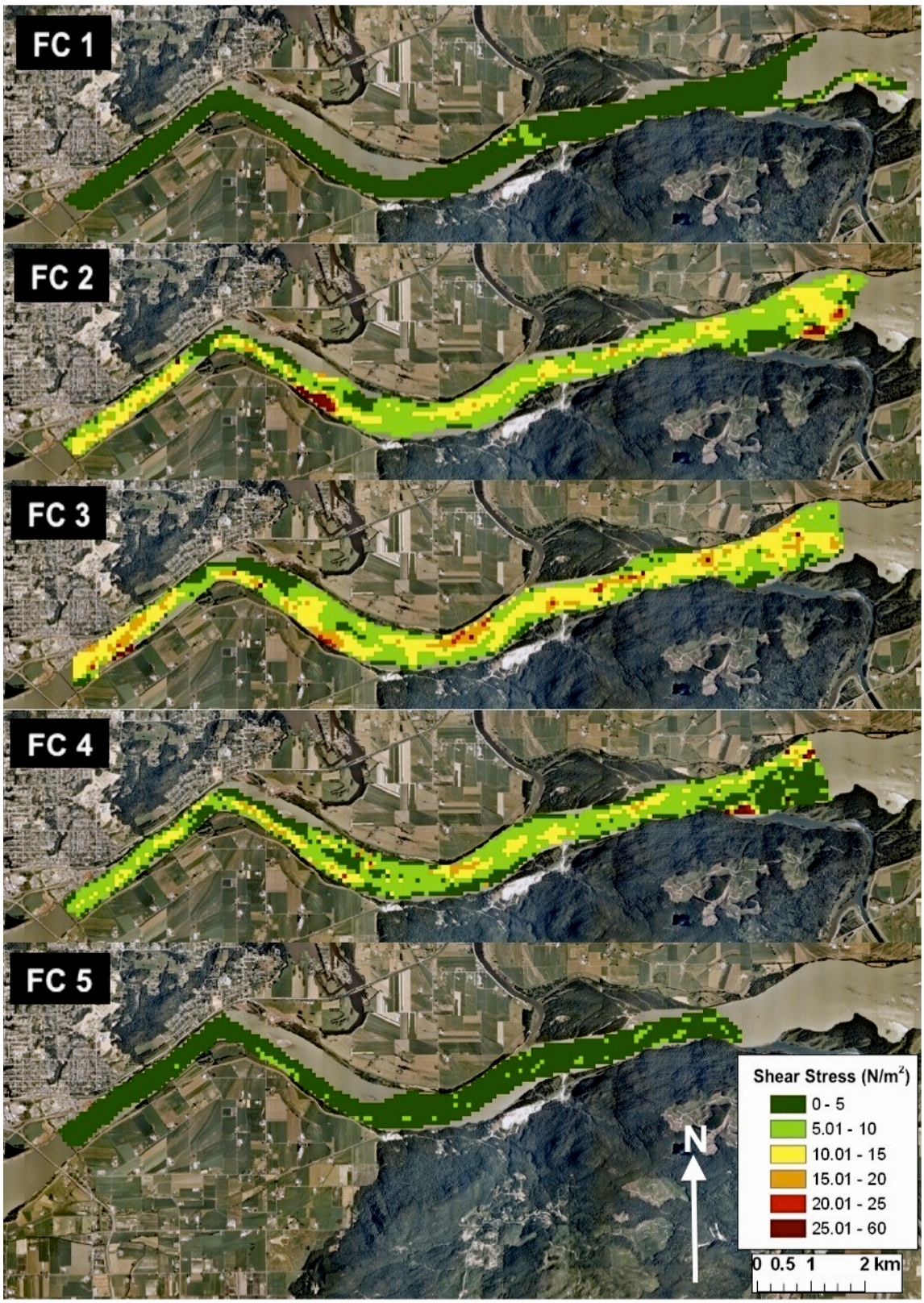

Figure 31: Spatial representation of shear stress for all field campaigns in 80-m resolution.

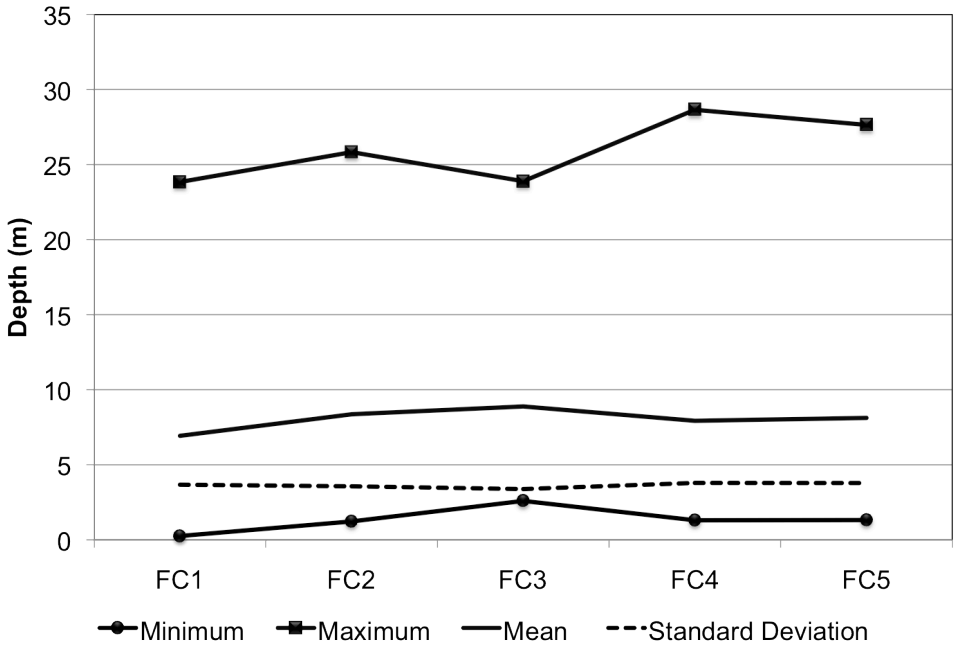

Figure 32: Descriptive statistics for depth maps.

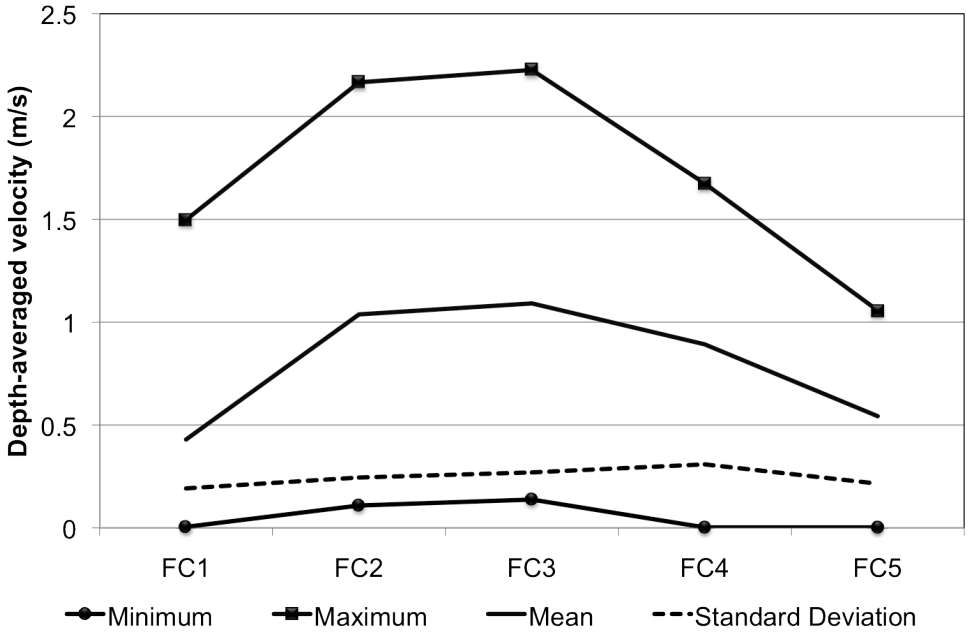

Figure 33: Descriptive statistics for depth-averaged velocity maps.

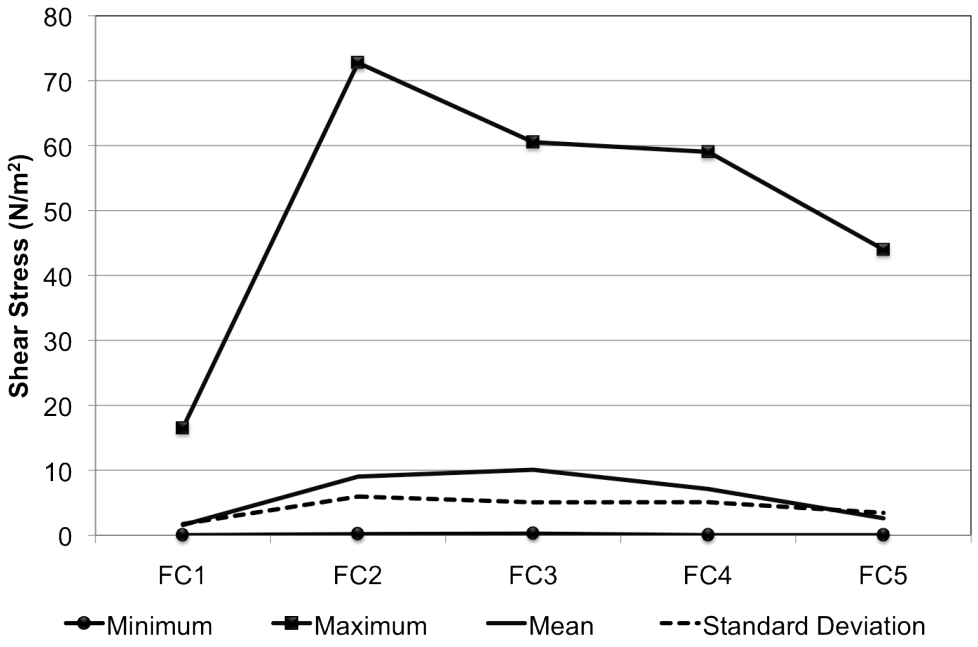

Figure 34: Descriptive statistics for shear stress map

4.3 Suspended Sediment Transport Through the Transition

Both suspended-sediment concentration maps based on water-corrected backscatter (top) and sediment-corrected backscatter (bottom) are presented in Figure 35. These maps are shown in the same scale, and display very similar patterns, suggesting that the patterns are not dependent on the correlation technique. The main difference between these different correlations of SSC is that the minimum and maximum values are exaggerated in the sediment-corrected maps because of the steeper slope of the relation. This exaggeration is most evident in the Hatzic bend section of the river.

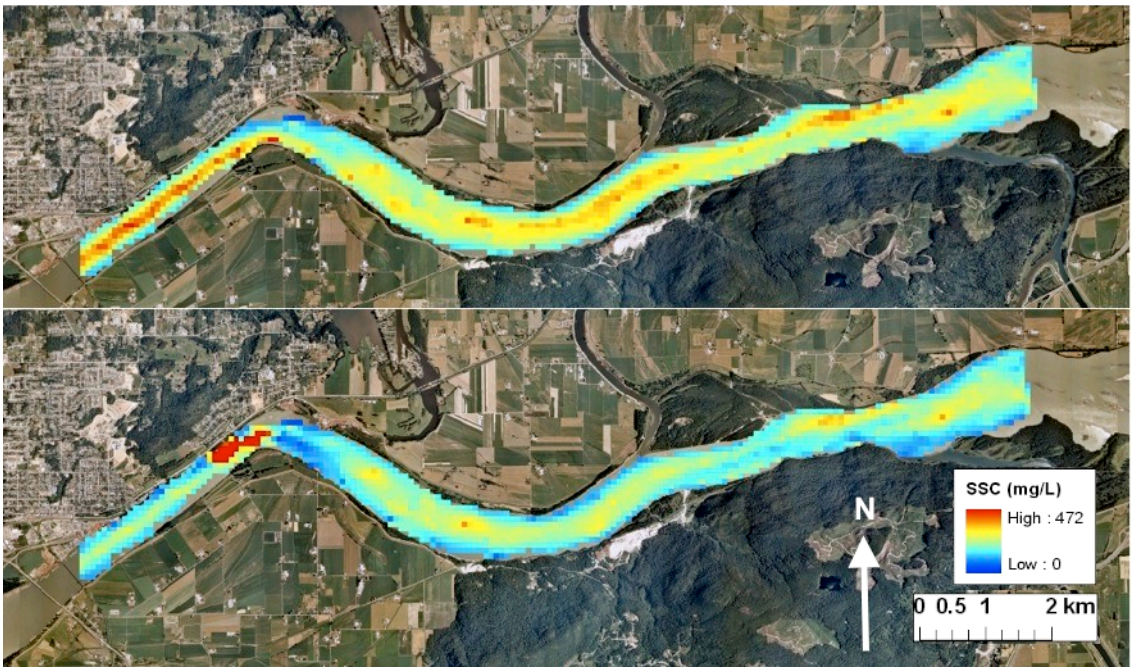

Figure 35: Suspended-sediment concentration maps from field campaign 3. Top map calibrated with water corrected backscatter, bottom map calibrated with sediment corrected backscatter.

Maps of suspended-sediment concentration (Figure 36) and suspended-sediment flux (Figure 37) illustrate suspended-sediment transport through the gravel-sand transition. Summary statistics, presented in Figure 38 and Figure 39, give the maximum, minimum, mean, and standard deviation of the suspended sediment transport maps.

High suspended-sediment concentration occurs in the channel north of Yaalstrick Bar, where depth and velocity are low. In addition, high concentration values are evident along the sinuous thalweg. During high flows SSC increases as it passes Hatzic Bend, in the Mission reach. During low flow SSC decreases downstream, and the highest concentration occurs near Yaalstrick Bar and just downstream of the Vancouver Sand and Gravel mine. High concentrations extend over the head of Hatzic Bar but not the tail, a pattern that explains why

the tail is not infilling (see the depth map in Figure 29). The highest SSC occurred during the third field campaign downstream of Hatzic Bend where the depth and velocity is high and the bed consists of sand only. The highest mean SSC for the entire reach occurred during the third field campaign and is 242 mg/L with a standard deviation of 68.8 mg/L.

The suspended-sediment flux is high along the sinuous thalweg mimicking the pattern of elevated velocity and shear stress shown in the maps in 4.2. However, it is low in the gravel-bedded portion of the river, and high in the sand-bedded reach downstream of Hatzic bend. In addition, the sediment flux per unit width increases downstream as the width declines. The highest mean flux is seen during FC 2 and FC 3 and is $0.8x10^{-3}$ m^2/s with a standard deviation of $0.6x10^{-3}$ m^2/s for both.

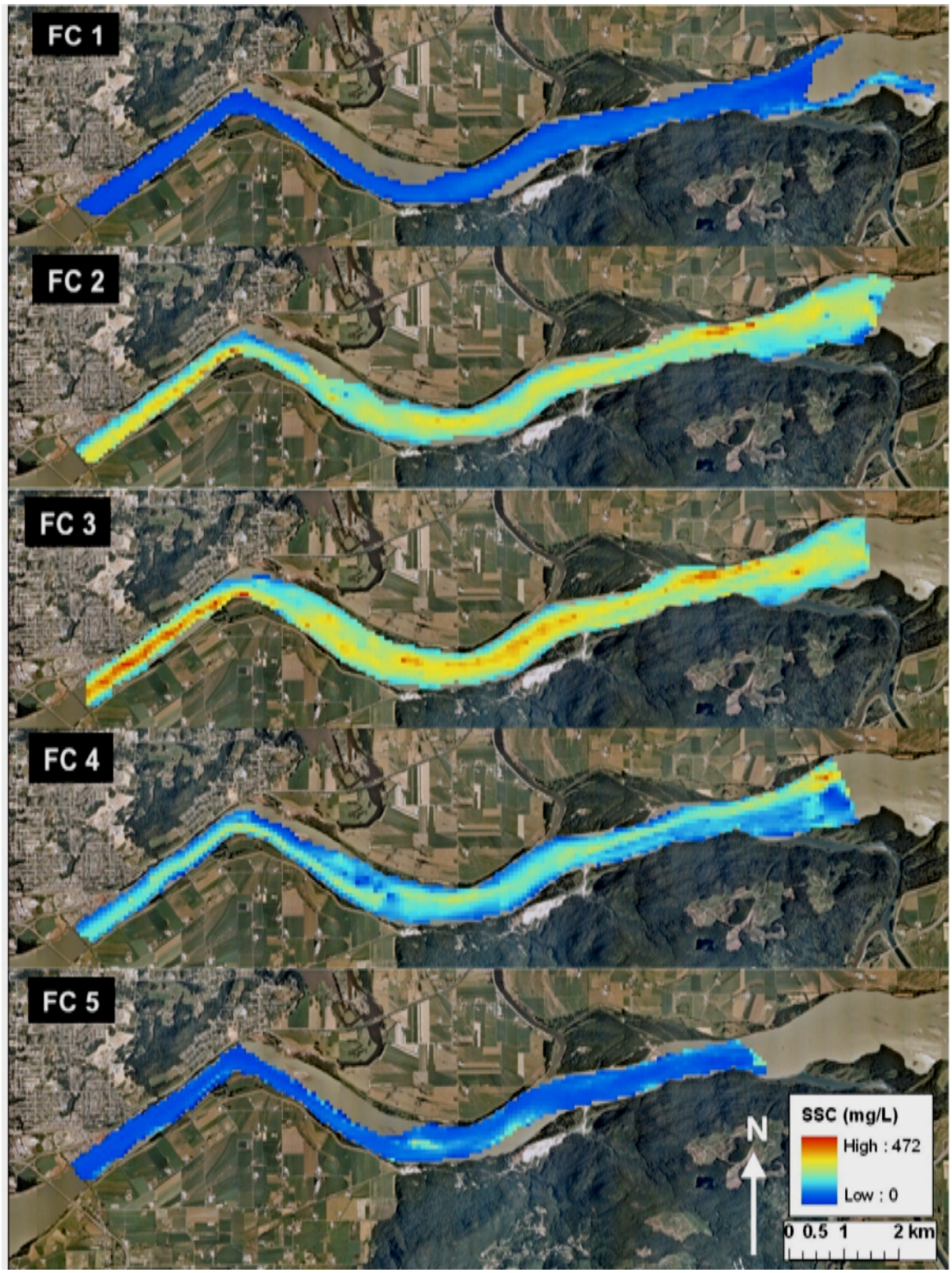

Figure 36: Spatial representation of suspended-sediment concentration calculated from water-corrected backscatter for all field campaigns in 80-m resolution

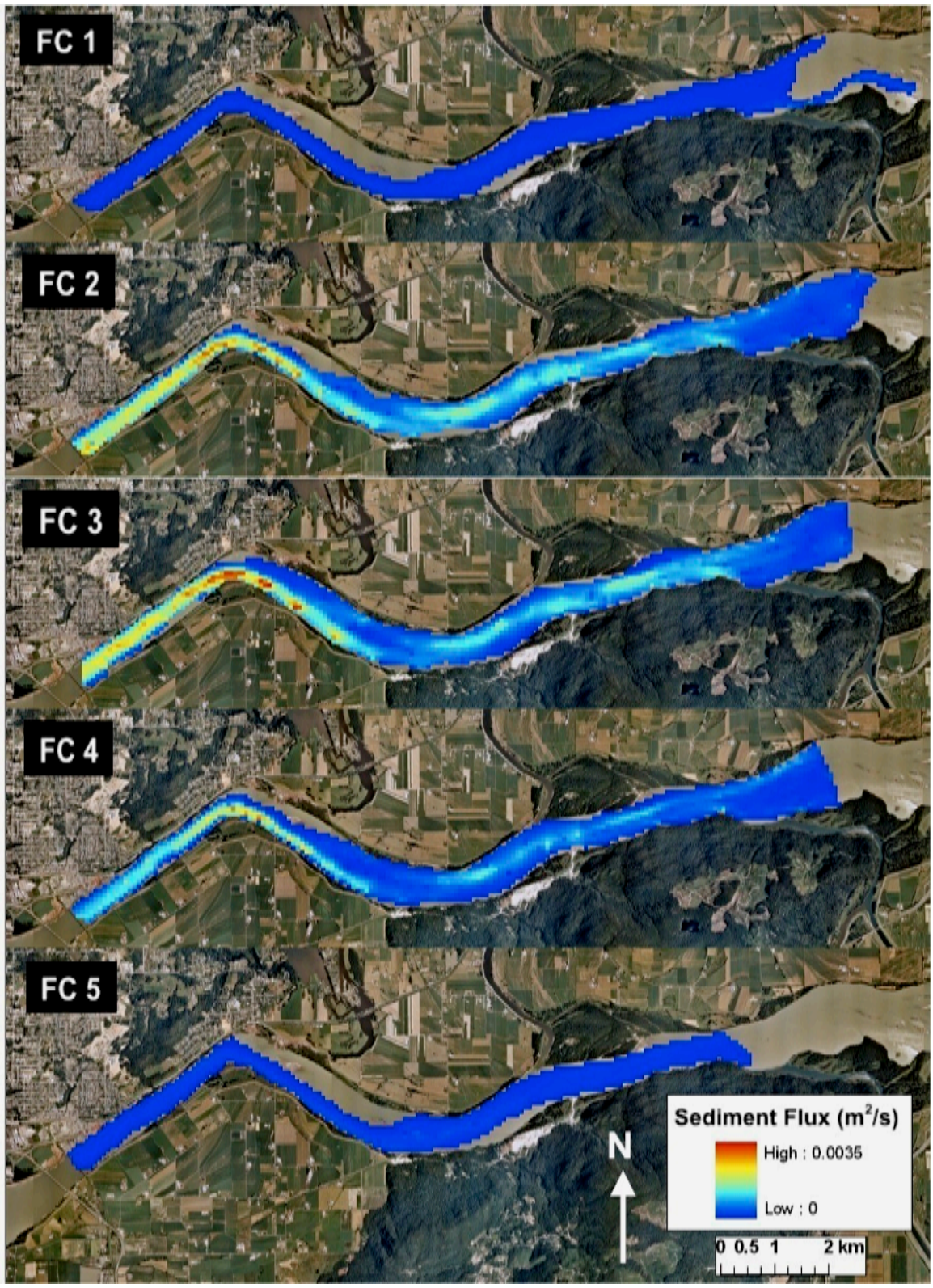

Figure 37 Spatial representation of suspended-sediment flux for all field campaigns in 80-m resolution.

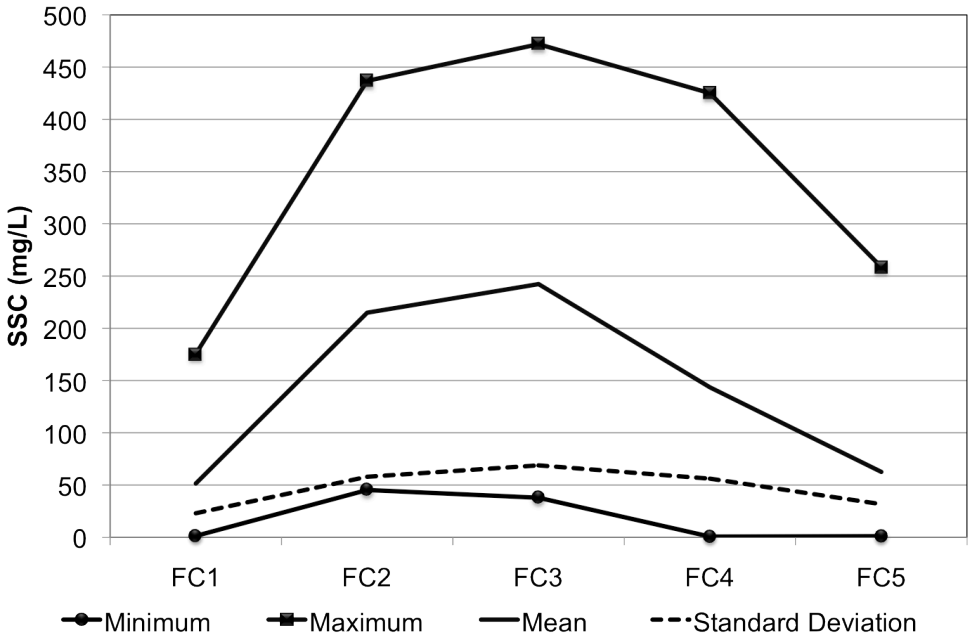

Figure 38: Descriptive statistics for suspended-sediment concentration calculated from water-corrected backscatter maps.

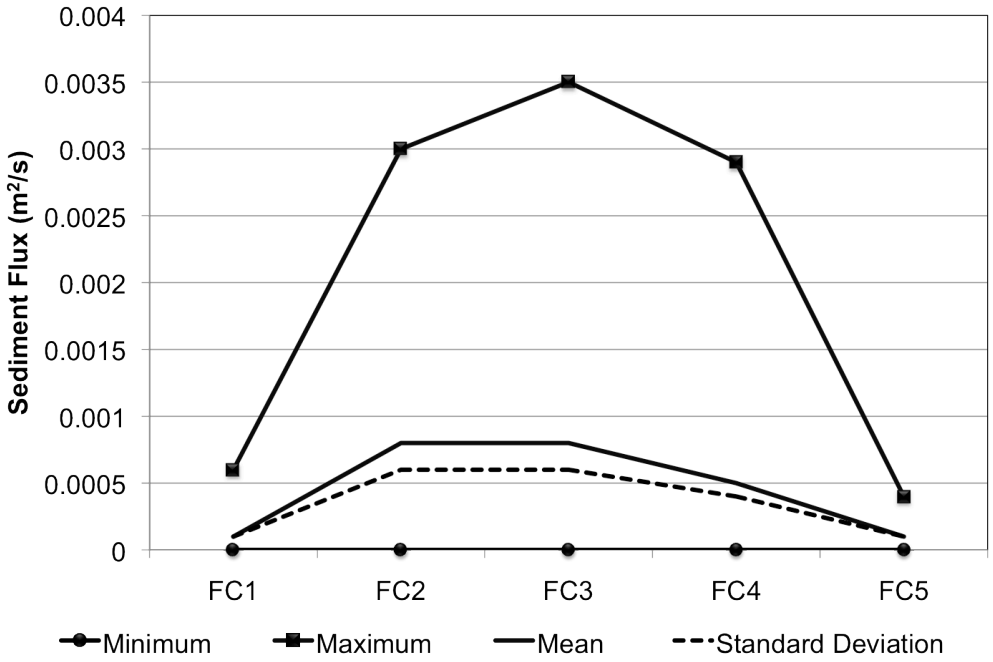

Figure 39: Descriptive statistics for suspended-sediment flux maps.

The SSC and suspended sediment-flux maps provide information on the total concentration and flux. Grain sizes cannot be inferred. Figure 40 provides locations of LISST measurements from the first (low flows) and third (freshet) field campaigns that are at approximately the same locations. Figure 41 and Figure 42 show depth-averaged concentrations, mean grain-size, and D_{16}, D_{50}, D_{84} from these locations.

At low flows during the first field campaign, concentration and grain size increase downstream to Sumas Mountain, and then decrease downstream to Hatzic Bend. They increase through Hatzic bend and decrease again at Mission. During high flows the same pattern is observed, however concentrations peak near Mission. During the first field campaign mean and median grain sizes of the suspended load are larger than during freshet flows in the third field campaign. This occurs because there is significantly more fine washload material coming from the drainage basin during high flows which causes the mean and median grain sizes to be much smaller.

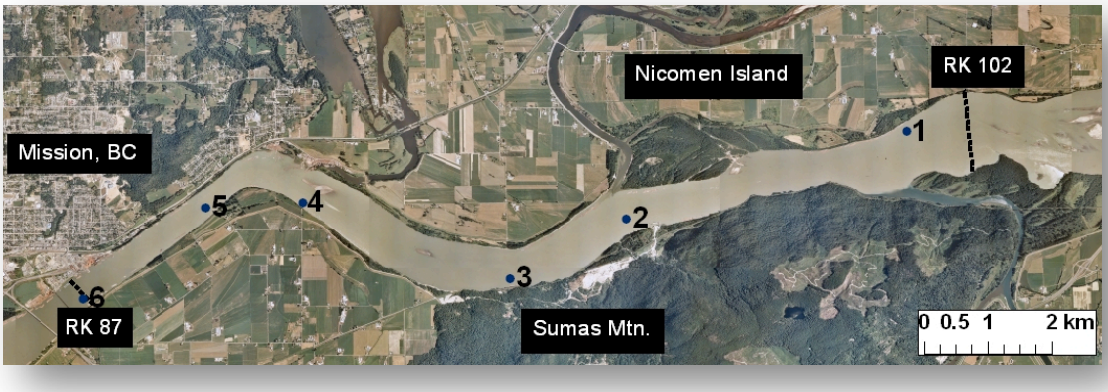

Figure 40: LISST sample locations for field campaign 1 and 3.

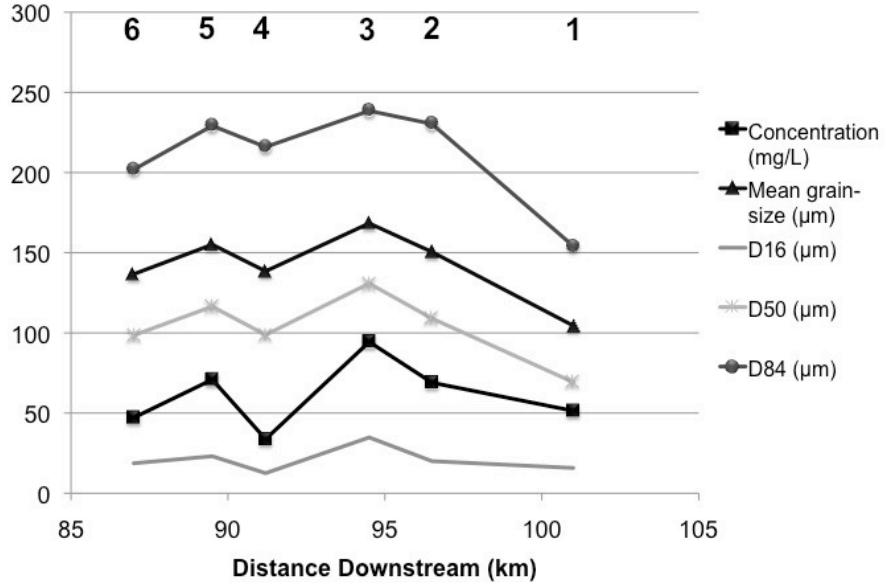

Figure 41: LISST suspended-sediment parameters from field campaign 1.

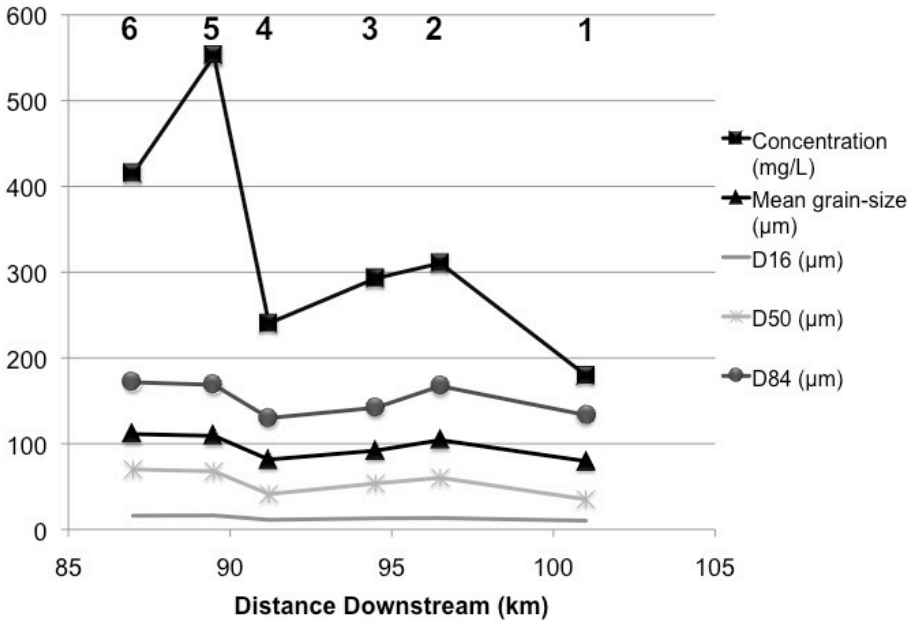

Figure 42: LISST suspended-sediment parameters from field campaign 3.

Suspended-sediment concentration profiles are presented in Figure 43 and show changes in concentration with depth. During low flows concentration does not vary much with depth, because the overall suspended-sediment

concentration is low. The vertical gradient in concentrations is greater at high flows because there is more bed material entrainment due to the increase in shear stress which entrains coarser bed material. The largest vertical gradient occurs downstream of Hatzic bend. The gravel-bedded reach displays a smaller vertical gradient in SSC and smaller concentrations than the sand bedded reach near Mission.

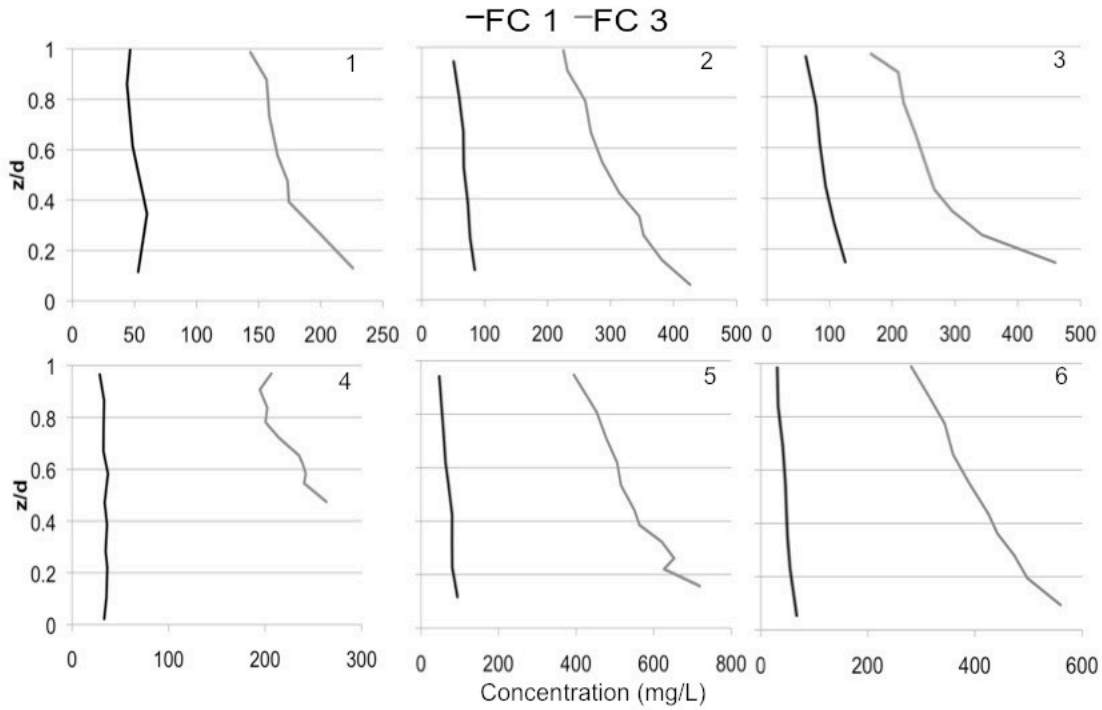

Figure 43: LISST profile concentrations for field campaign 1 and 3.

Grain size percentile profiles are shown in Figure 44 for the six points downstream for field campaigns 1 and 3. The steepest vertical gradient in D_{50} occurs in the profile just downstream of Sumas Mountain for all percentiles. Also, D_{50} is larger in FC1 than FC3 because there is much more fine sediment near the bed at high flows. Grain size increases towards the bed, particularly at high flows. The vertical gradient in D_{50} is similar at both high and low flows. The

vertical gradient in D_{90} is steeper at high flows due to the entrainment to suspension of coarser bed material. This does not occur for the D_{16} as most of this material is washload and is well mixed vertically in the channel.

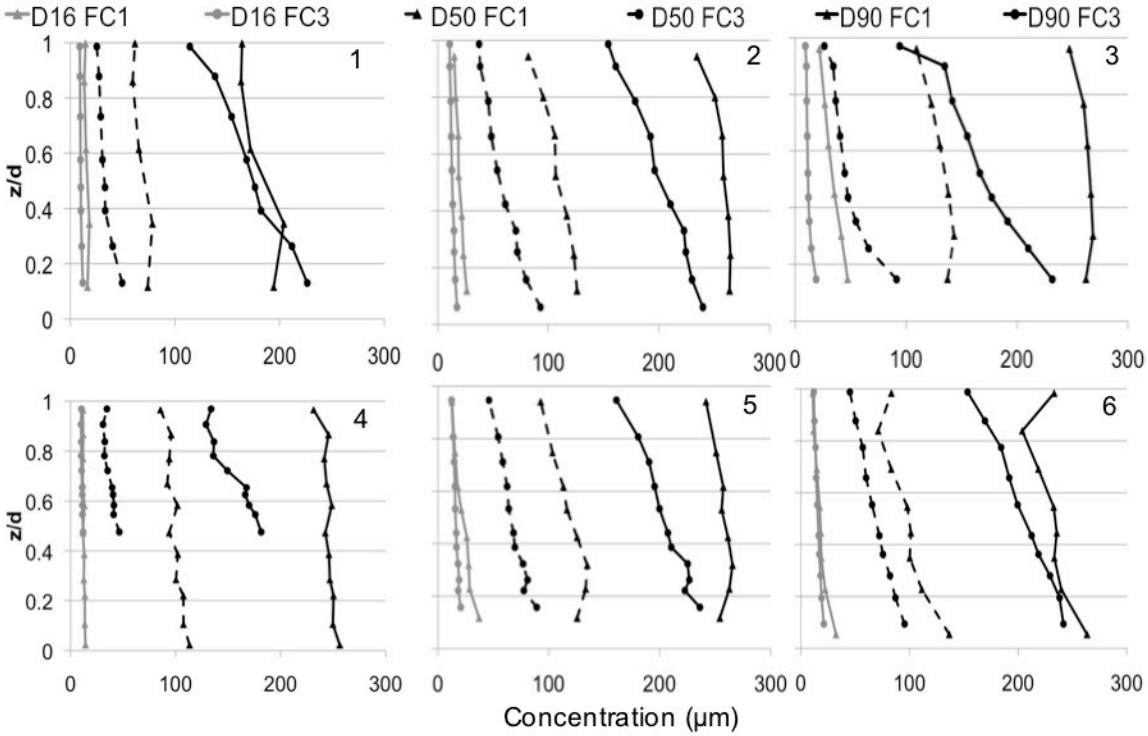

Figure 44: Grain size percentile profiles for field campaign 1 and 3.

4.4 Downstream Variability of Fluid Flow and Sediment Transport

Sample points were selected every 0.5 river kilometres from river kilometre 87 to river kilometre 100 along the thalweg of the river to examine downstream changes in flow and sediment transport. Depth, depth-averaged velocity, shear stress, SSC, and sediment flux were extracted from these points. Total suspended-sediment flux was also calculated for every 0.5 kilometres by adding all pixel values across a cross-section oriented perpendicular to the channel centreline. Figure 45 displays the location of each point.

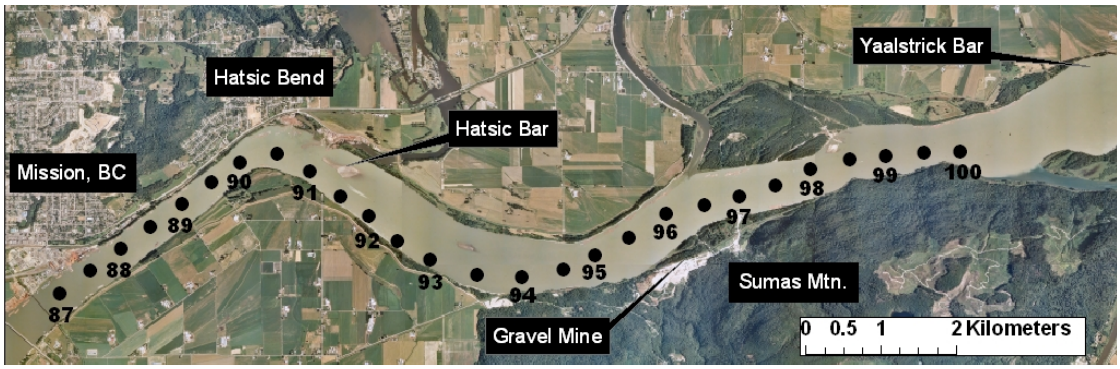

Figure 45: Location of sample points where flow and sediment parameters were extracted to observe downstream patterns.

Both spatial downstream patterns and temporal changes can be observed in these results. The extracted values from these locations are presented in Figures 47 to 51, and capture spatial changes in flow parameters and suspended-sediment transport for each field campaign.

Depth (Figure 46) follows the same pattern during all field campaigns although the highest depth values are observed during the high flow campaigns (FC 2, FC 3, FC 4). Depth-averaged velocity (Figure 47) increases just downstream of Yaalstrick Bar, then steadily decreases to the Sand and Gravel mine. Downstream of the mine velocity slightly increases until the downstream end of Sumas Mountain where a dramatic drop in velocity is observed. Another dramatic velocity drop is seen in Hatzic bend. High flow velocities (FC 2, FC 3, FC 4) are roughly double low flow velocities (FC 1, FC 2).

A difference between high flows and low flows is visible in the downstream shear stress values (Figure 48). During high flows (FC 2, FC 3, FC 4), shear stress is high downstream of Yaalstrick Bar and drops just downstream of Sumas Mountain and also right before Hatzic bend. A subtle downstream decline in

shear stress is observed during low flows (FC1, FC 5). In addition, at lows flows, there is much less variability in shear stress values.

Suspended-sediment concentration (Figure 49) also displays different patterns at high and low flows. During high flows low concentrations are seen just upstream of the Sand and Gravel mine and upstream of Hatzic bend. High concentrations are located downstream of the Sand and Gravel mine and at the downstream end of the gravel-sand transition reach at Mission. During low flows in April (FC 1) there is a steady decrease in SSC with a visible drop near Hatzic bend. During low flows in October/December (FC 5), concentrations peak at Sumas Mountain and a decline at Hatzic bend.

Suspended-sediment flux (Figure 50) increases downstream with dramatic drops just downstream of the Sand and Gravel mine and just upstream of Hatzic bend. In addition, there is a dramatic increase between the downstream end of Sumas Mountain and Hatzic Bar. During low flows, sediment flux peaks upstream of Hatzic bend and declines downstream of Hatzic bend.

Total suspended-sediment flux (Figure 51), which was calculated from cross-sectional sums of the suspended-sediment flux, fluctuates downstream during high flows but there are no significant differences in total flux in the gravel-bedded and sand-bedded sections of the river, which indicates that the river is maintaining sediment continuity throughout the transition reach. At low flows there seems to be a slight decrease downstream with higher values in the gravel bedded section near Yaalstrick Bar. During high flows there is a drop in total flux downstream of Sumas Mountain indicating that deposition is occurring, followed

by a sharp increase at Hatzic Bend where values peak. Total flux then levels off in the Mission reach where bed material is being suspended from the sand bed.

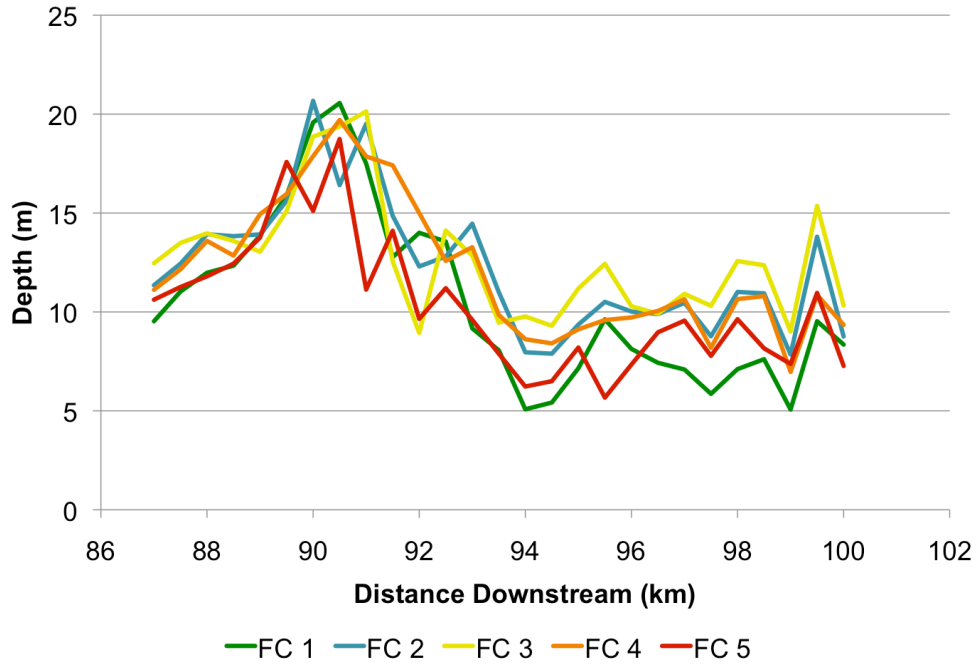

Figure 46: Downstream changes of depth through the transition reach.

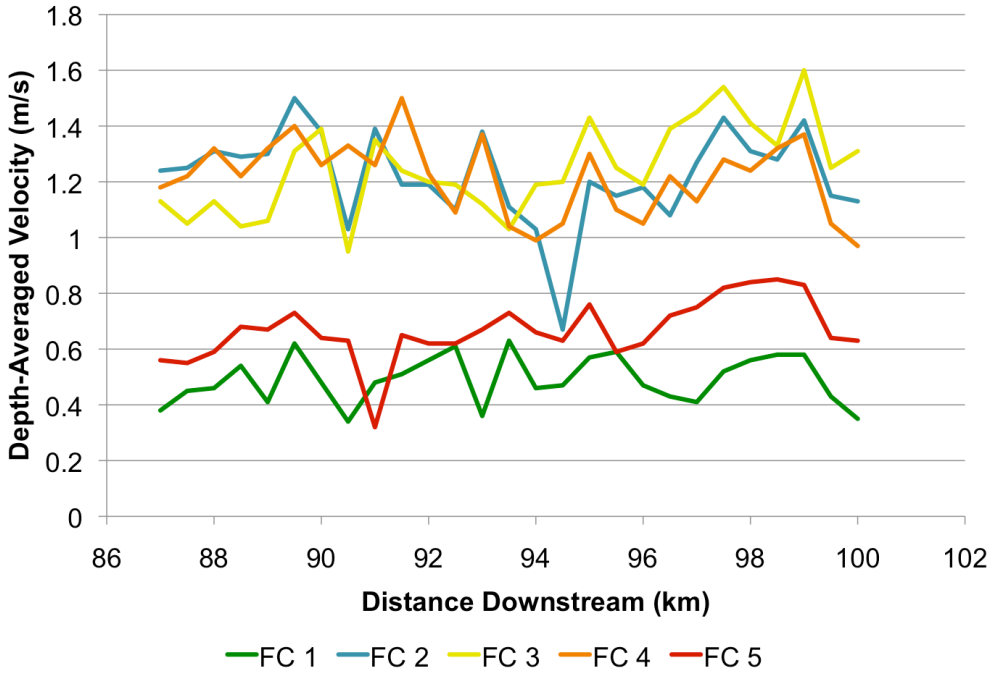

Figure 47: Downstream changes of depth-averaged velocity through the transition reach.

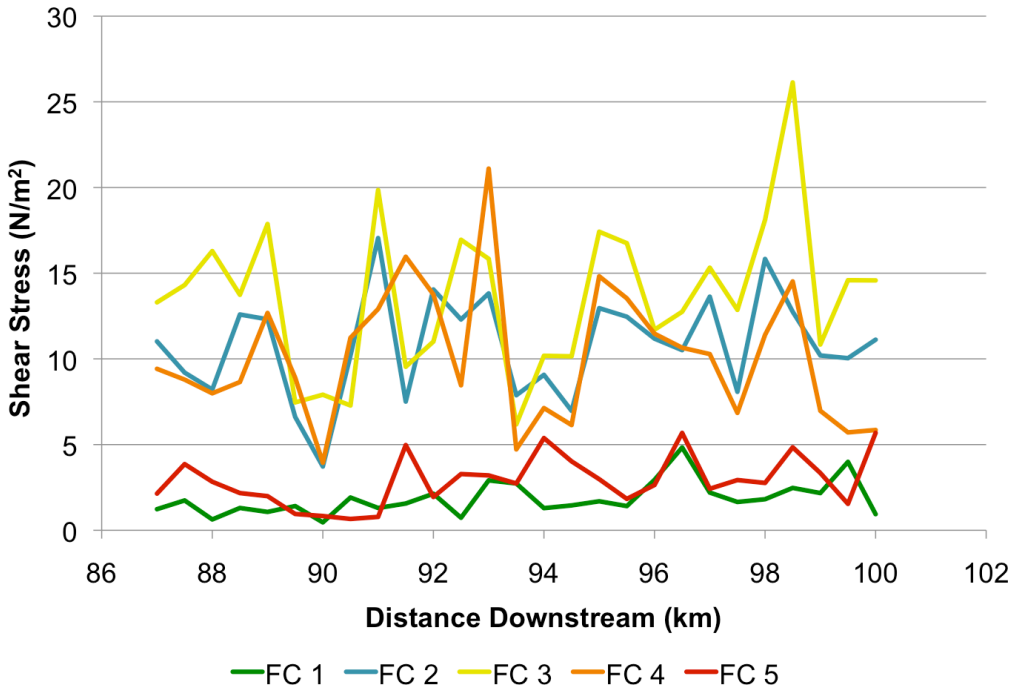

Figure 48: Downstream changes of shear stress through the transition reach.

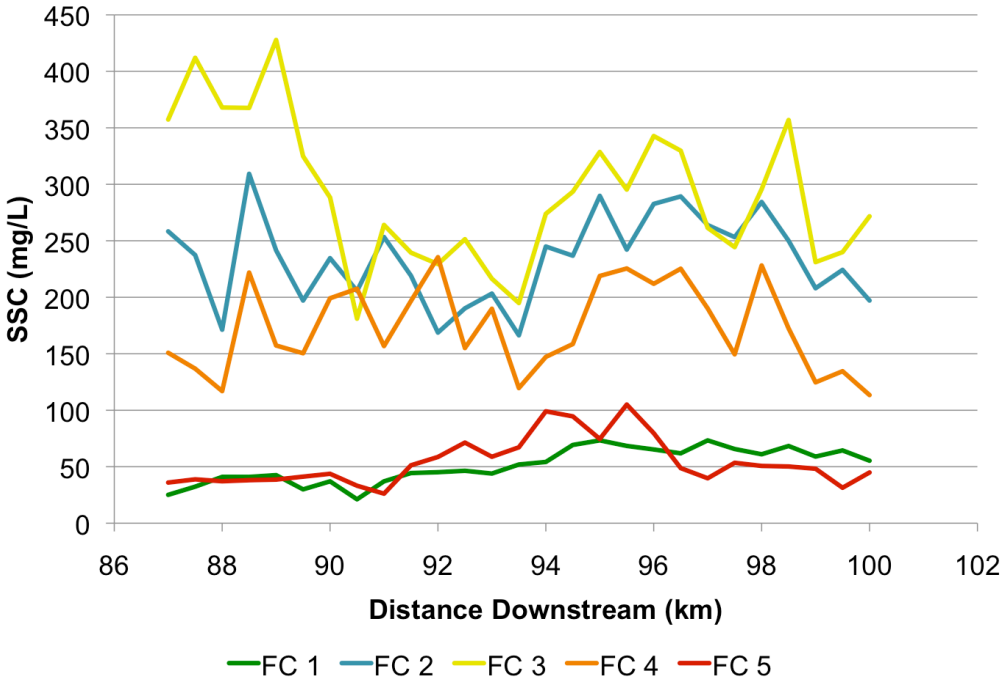

Figure 49: Downstream changes of suspended-sediment concentration through the transition reach.

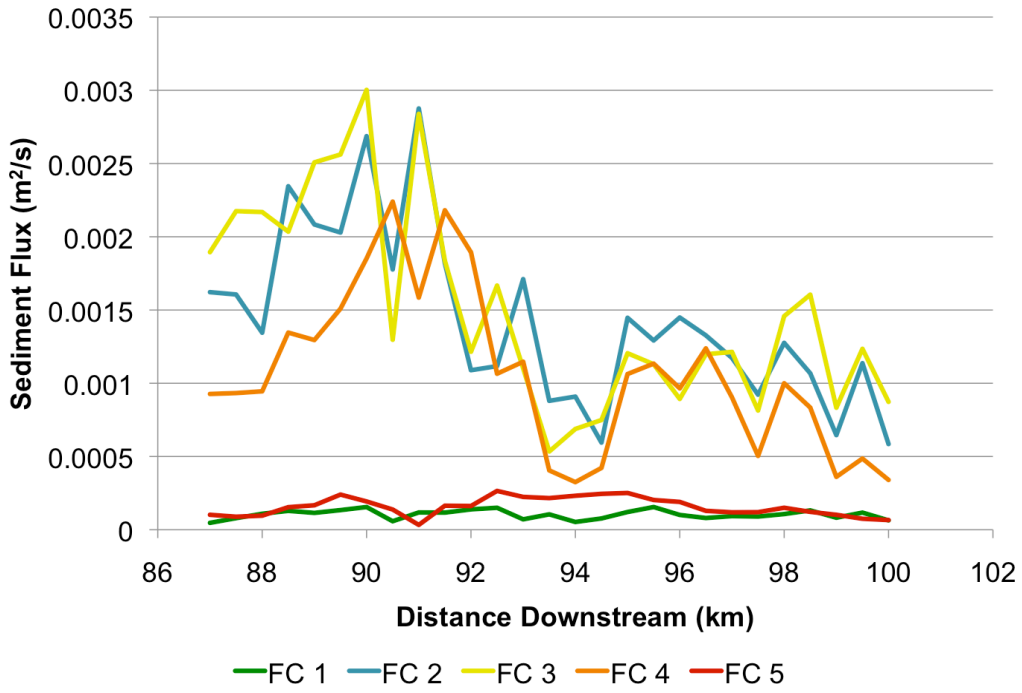

Figure 50: Downstream changes of suspended sediment flux through the transition reach.

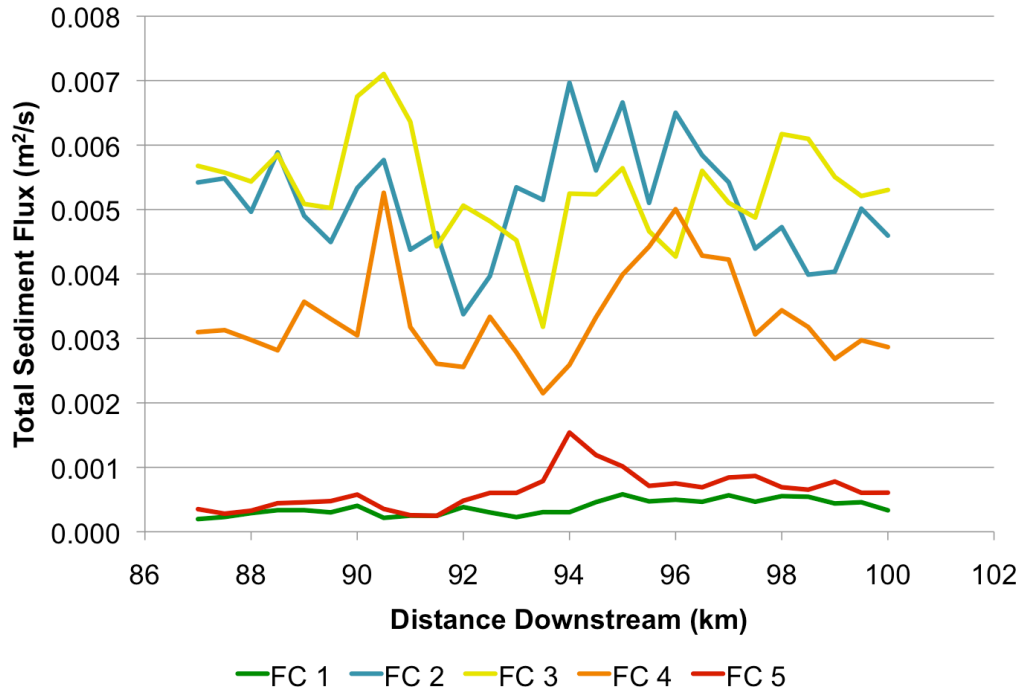

Figure 51: Downstream changes of total suspended sediment flux through the transition reach.

The lack of downstream gradient in shear stress in the gravel-sand transition reach was surprising and was explored in more detail by examining all the shear stress values. Shear stress values were plotted up against easting, which declines downstream, because the data are not indexed against river kilometre directly. All shear stress values from the maps were extracted and plotted against the easting to determine whether shear stress values change downstream. The rising limb field campaigns (1-3) and falling limb campaigns (3-5) are shown in Figure 52. A few erroneous data points were removed from these graphs because they exceeded 30 N/m^2. The mean and standard deviation for all campaigns can be seen in Table 4-3.

Field campaigns 1 and 5 follow a similar downstream pattern. Shear stress for the low flow campaigns seems to vary less in the downstream direction than for higher flows. High flow shear stress shows downstream periodicity, which reflects the sinuous thalweg and the bar-pool sequence downstream. The high flow shear stress also seems to display a patchy pattern much like the shear stress map (Figure 31) and does not show definite downstream increases or decreases.

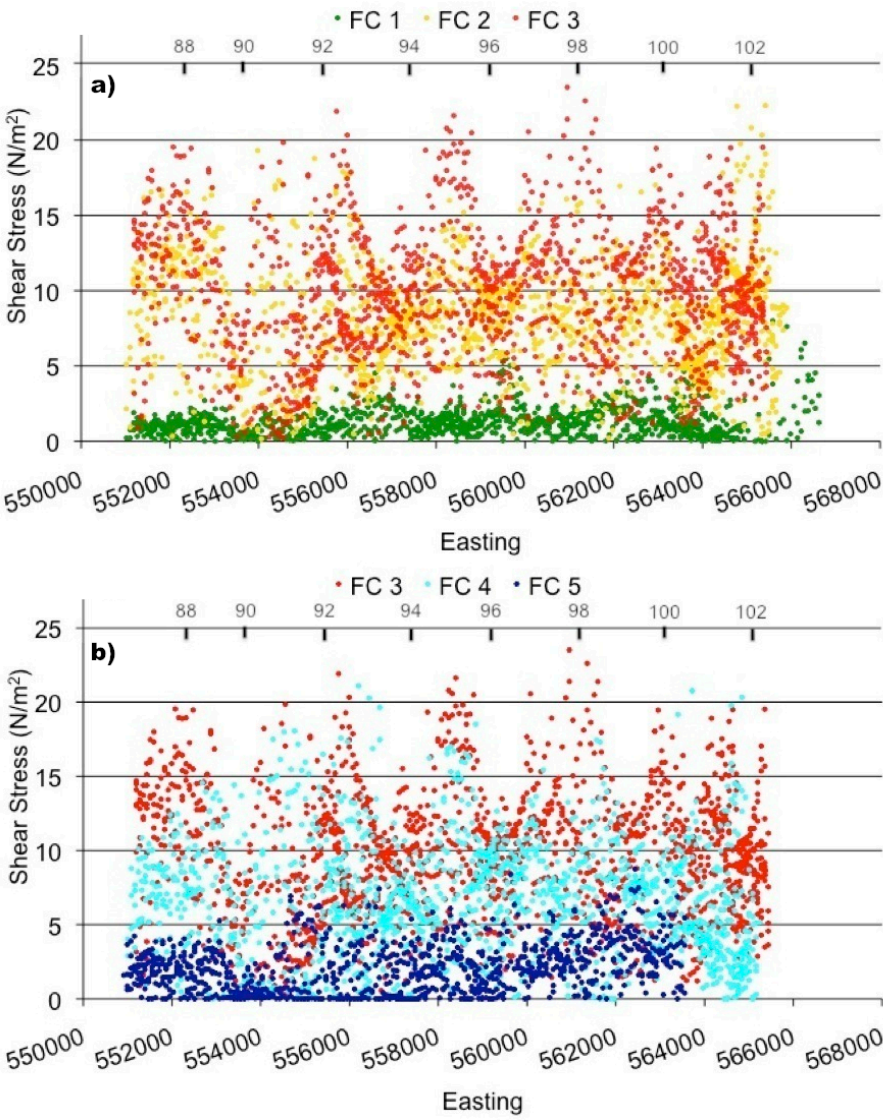

Figure 52: Shear stress values against easting for the: a) rising limb of the hydrograph (field campaigns 1-3), and b) falling limb of the hydrograph (field campaigns 3-5). River kilometres marked by lines.

Table 4-3: Mean and standard deviations for shear stress plots for all field campaigns.

Field Campaign	Mean	Standard Deviation
1	1.34	1.08
2	8.29	3.72
3	9.55	4.19
4	6.84	3.96
5	2.21	1.69

In order to examine how the shear stress patterns influence sediment mobility. The non-dimensional shear stress (Shields number) was calculated using:

$$\tau_* = \frac{\tau}{(\rho_S - \rho)gD} \tag{16}$$

where τ_* is the Shields number, τ is dimensionless shear stress, ρ_s is the density of the sediment (2650 kg/m^3), ρ is water density (1000 kg/m^3), g is acceleration due to gravity (9.81 m/s^2), and D is sediment grain size.

The Shields number was calculated for grain sizes from 0.3 mm to 64 mm and plotted to determine what size of sediment is in motion for the first and third field campaigns (Figure 53). The critical shear stress is assumed to be 0.03 for the 0.3 mm sand that makes up the bed at Mission, and 0.045 for a gravel mixture (Miller et al., 1977; Yalin & Karahan, 1979). The figures indicate that during the low stage (FC 1) 2 mm and 4 mm coarse sand to fine gravel are at the threshold of motion and sand finer than 1 mm is mobile. During high flows (FC 3) 16 mm fine gravel is at the threshold of motion while fine gravel smaller than 16 mm is mobile. This is consistent downstream with a drop in sediment size right before Hatzic bend where at low flows 1 mm coarse sand is at the threshold and during high flows 8 mm fine gravel is at the threshold.

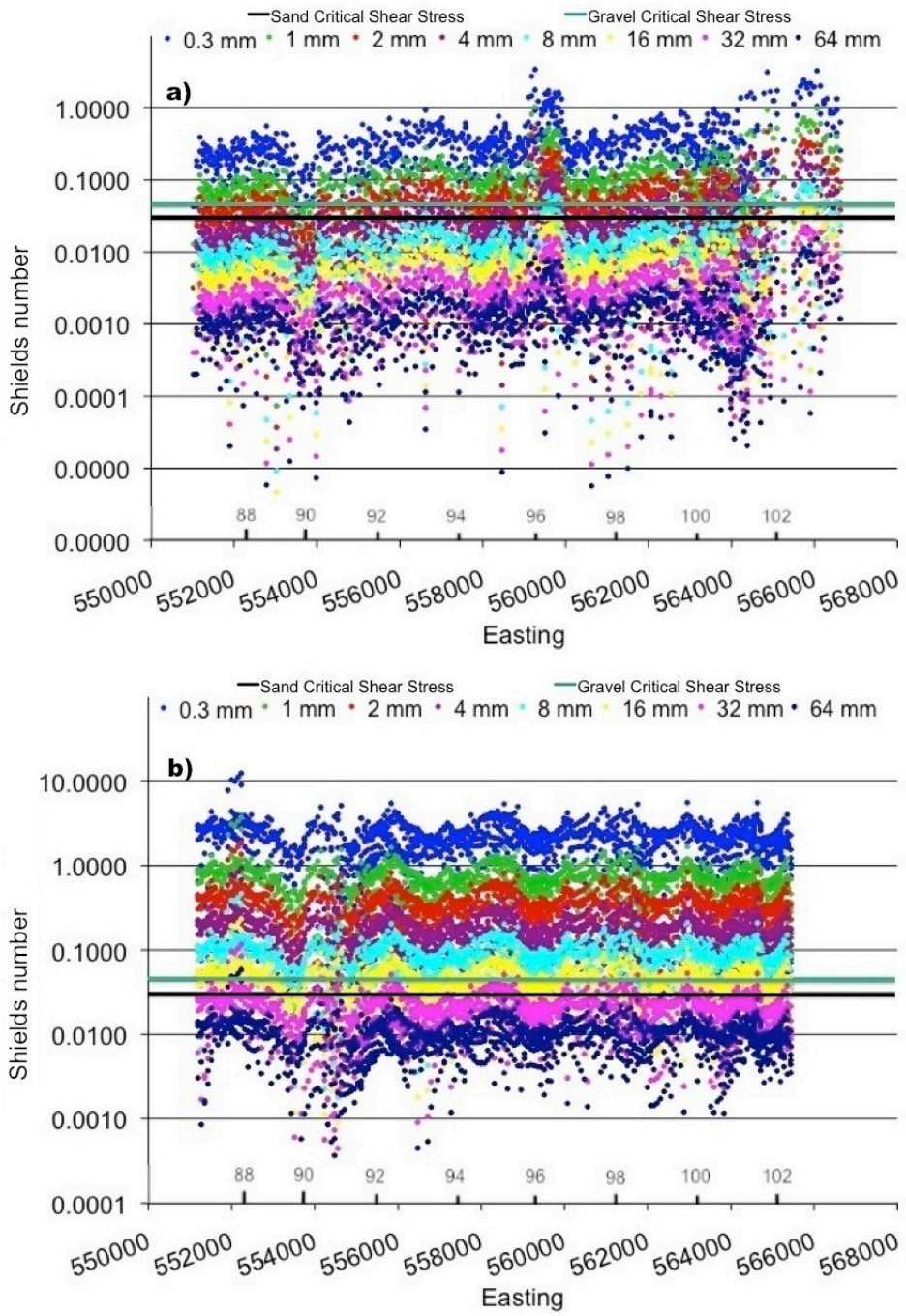

Figure 53: Shields number for medium sand to fine gravel for a) field campaign 1 and b) field campaign 3.

The mobility of 0.3 mm sand as suspended material and as bedload is displayed in Figure 54 for field campaign 1 and 3. This diagram shows the ratio of the setting velocity divided by shear velocity (u_s / u_*) to predict suspended

material mobility (Bagnold, 1966; Van Rijn, 1984), and the critical dimensionless shear stress divided by dimensionless shear stress (τ_{*_c}/τ_*) to predict bedload mobility. If τ_{*_c}/τ_* is <1, the sand is mobile as bedload and if u_s/u_* <1, the sand can be suspended. If either of these values is greater than 1, the particles cannot be moved in that particular transport mode. During the low flow campaign (FC 1) 0.3 mm sand can be transported as bedload, but is at the threshold for suspension. During high flows (FC 3) 0.3 mm sand can be transported as both bedload and suspended load.

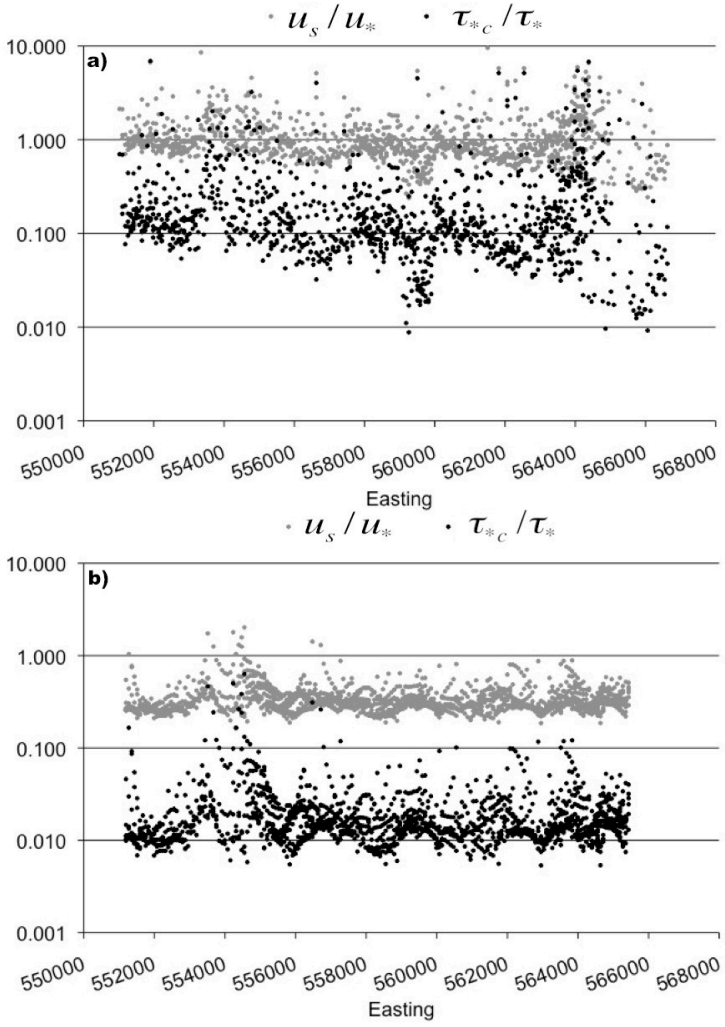

Figure 54: Suspended sediment and bedload mobility for 0.3 mm sand for a) FC 1 and b) FC3

5: DISCUSSION

5.1 Introduction

It is clear from the maps and corresponding figures in the results section, that most of the sediment transport occurred during the second and third field campaigns right before the freshet. These periods also had the highest flow, velocity, and shear stress throughout the transition reach. The concentration of sediment during the freshet campaign in early June was an order of magnitude larger than during the first and last campaigns in April and October/December, respectively. The mean and median suspended grain-size values were ~25-80 μm larger during low flows than during the freshet. This is because more fine sediment was moving through the channel during high flows, and not due to more coarse sediment moving in the channel at low flows. But coarser sediment must make up a smaller proportion of the total sediment flux at high flows for the suspended material to be finer.

Spatially, clear downstream gradients of depth-averaged velocity (Figure 47), shear stress (Figure 48), and SSC (Figure 49) do not exist and highest values follow the sinuous thalweg. At high flows, shear stress values at the upstream end of the study area near Sumas Mountain are just as high as in the downstream end of the reach near Mission. Suspended-sediment concentration follows the same pattern and has even higher values in the downstream end of the transition reach during the third field campaign.

The data have also demonstrated that during all field campaigns the median fine fraction (0.3 mm) of the sand-bedded section of the Fraser River is mobile. During the high stage field campaign the largest mobile grain-size is 8 mm, according to the Shields number, which is significantly smaller than the median coarse gravel fraction.

So, based on the Shields number threshold, coarse gravel should not be mobile, even at the high flow in the gravel-bedded portion of the river. But coarse gravel must be mobile at some time; otherwise it would not be in this part of the river. The lack of coarse gravel mobility may occur because the 2009 freshet was not large compared to the historical record (Figure 6). In fact, the flow was equivalent to the mean annual flow. Coarser gravel may only be mobile at flows well above the mean annual flood. Or, gravel may be mobile at lower flows in this part of the river because of the sand surface coverage. Several researchers have demonstrated that the presence of sand can mobilize an otherwise immobile gravel bed. Wilcock (1998) and Wilcock and Kenworthy (2002) demonstrate a reduction of the critical Shields number for entrainment of ~3.5x as the percent sand coverage increases. Gravel transport increases by an order of magnitude as the sand content increases from 6% to 34% (Wilcock et al., 2001). Coarse fraction transport has also been shown to increase with fine gravel loading (Venditti et al., 2010a; Venditti et al., 2010b).

5.2 Dominant Controls of the Gravel-Sand Transition

The location of the Fraser River gravel-sand transition is identified as externally controlled by a dramatic change in slope that occurs at Sumas

Mountain and with a local base-level control which is the upstream backwater effect caused by the ocean tides. Venditti et al. (2008; 2010c) suggest that, as a result of a loss of competence, gravel transport ceases and only sand can be transported. Thus, they believe there should be strong gradients in suspended-sediment concentrations and grain size from Yaalstrick Bar to Mission. In addition, with a loss of competence, velocity, shear stress and suspended sediment flux should decrease downstream.

The highest flows are observed near Yaalstrick Bar, where the river is still gravel-bedded. There are abrupt changes in the velocity (referred to as breaks) visible on the maps (Figure 30) and in the extracted downstream profile points (Figure 47) for all field campaigns. This decrease in velocity can be seen around river kilometre 96, located near the gravel-mine. For the third field campaign (the freshet flow) depth-averaged velocities follow the same pattern but this break is observed slightly downstream at roughly river kilometre 93, due to higher flows. This pattern is also evident in the shear stress values, SSC and sediment flux maps for all flows (Figure 48-Figure 50). However, this break in shear stress is observed further downstream (~1km) from where the velocity and shear stress breaks occur.

This rapid decrease in flow and SSC is also supported by the LISST data samples (Figure 41 & Figure 42). There is a dramatic decrease in suspended-sediment concentration, suspended mean and median grain-sizes between river kilometres 94 and 91, which are located near the gravel-mine and before Hatzic bend, respectively. This change in grain-size is more prominent during low flows.

These data trends are concurrent with the dramatic change in slope that takes place at Sumas Mountain, and supports the work by Venditti et al., (2008; 2010c) asserting that a loss of competence occurs just downstream of Sumas Mountain between river kilometres 93 and 96. This pattern is observed during all flows measured. This phenomenon is more pronounced during low flows, suggesting that the sand-bed portion of the transition is supplied during these high flow conditions, as only very coarse sand is able to come out of suspension in the break sections of the river downstream of Sumas Mountain.

During peak freshet flows it is highly unlikely that sand deposition occurs, because fine gravel >8 mm is predicted to be mobile in these conditions. This is also supported by the shear stress and suspended-sediment concentration observed in the downstream section of the reach which decrease slightly yet increase again downstream of Hatzic Bend (Figure 48 & Figure 49). The most obvious example evident is in SSC during the freshet. It is clear that after this break in slope near Sumas Mountain, where a visible decrease in velocity and SSC occurs, the river gains momentum and concentrations increase drastically downstream, reaching values much higher than elsewhere in the transition reach. In addition, the river narrows in the Mission reach causing channel constriction, which causes an increase in velocity and SSC as sandy bed material is entrained. This suggests that sand is being entrained and carried out of the gravel reach during peak flows in order to maintain the sand-bedded reach. There is evidence that this may be occurring in WSC gauging station records that

show metre-scale seasonal changes in bed elevation in the gravel bedded reach (Sichingabula, 1993) that may be sand deposition.

Tidal base-level control is also assumed to affect the location of the transition. The upstream extent of the backwater effect caused by the tides coincides with this break in slope. The timing of the field campaigns were selected to observe periods of high sediment transport and focused on falling tides; therefore, the dataset is unable to observe the sediment transport during rising tides. During the freshet the tidal influences are reduced and have less of an impact on sediment transport. However, during lows flows the winter tides can cause diurnal fluctuations up to 1000 m^3s^{-1} in discharge in Mission. During these peak tides it is possible that this base-level control can aid in supplying sand to the downstream end of the transition reach, but these high tide fluctuations are not frequent and high volumes of sediment transport are unlikely. The backwater effect caused by the ocean tides is a probable aid in maintaining the location of the transition rather than being the dominant control.

From the flow and suspended-sediment concentration data, it is clear that the major control affecting the location of the transition is the break in slope causing a loss of competence. The processes resulting in this phenomenon are a decrease in flow velocity and shear stress, a distrainment of gravel, and a continuous transport of sand.

5.3 Sorting Processes

Venditti et al. (2010c) believe the gravel-sand transition appears as a gravel front at the downstream end of Yaalstrick Bar. Existence of this gravel front is consistent with this data set due to the decline in bed slope, which causes a drop in shear stress where gravel bed motion comes to a halt.

Sorting processes control this abrupt gravel front. There are many suggestions as to what sorting processes actually occur in these environments. Ferguson et al. (1998) state that size sorting is enhanced in situations where a dramatic decline in slope occurs, because critical shear stress variance becomes larger to move different grain sizes as shear stress declines downstream. As this occurs, coarser particles are deposited and finer particles are selectively transported. The bed then becomes finer downstream as there is a reduced availability of coarser particles from upstream sediment supply. Ferguson (2003) builds on work by Wilcock (1998) suggesting that abruptness arises because the bed becomes more sandy. This is thought to occur because sand coverage increases the transport rates of both sand and to a lesser extent gravel, and relative to gravel, sand supply increases downstream. Therefore, transitions will be abrupt where critical sand coverage occurs on a gravel bed and where there are strong downstream gradients in sand coverage.

The results from this study support this notion proposed by Ferguson (2003) and Wilcock (1998). During all flows it is clear that there is a dramatic change in slope where shear stress, SSC, and suspended-sediment flux decreases past Sumas Mountain. Therefore, deposition is occurring in the break

section of the river which reduces the availability of coarse fractions. After this section shear stress and SSC increases again where this coarse fraction does not exist and only sand is suspended.

During all flows it is evident from these results that velocity, shear stress, and suspended-sediment concentrations are too high to allow 0.3 mm sand to come out of suspension and fine gravel motion does not cease also supporting the suggested gravel front theory.

Observations from previous work by Venditti et al. (2010c) indicate that throughout the transition reach there are areas where gravel appears in deeply scoured pools and on bar head immediately downstream of these pools. Samples from shallow trenches on Hatzic Bar indicate that the gravel surface grades into a gravel-sand mix with increasing sand content at depth. In addition, samples from the deepest part of the Hatzic Bend are composed of packed marine mud, which underlies Fraser River sediments. This suggests that Hatzic bend is scouring to the base of modern river sediments at high flows.

Venditti et al. (2010c) state that, between Yaalstrick Bar and Mission, sorting patterns caused by the superior mobility of gravel over sand, have lead to gravel patches through the apex of some river bends and gravel bar heads. They suggest that gravel deposition that occurs downstream of the gravel front is formed by particles ‘leaking out’ of the gravel bedded section of the river and moving into deep scour holes and bar heads.

This information suggests that during high flows gravel motion does not come to a halt downstream of Yaalstrick Bar. It is supported by critical shear

stress calculations indicating that gravel up to 32 mm could potentially be mobile along with the small downstream gradients of velocity and shear stress observed during high flows in this study. As sand and fine gravel coverage increases downstream of Yaalstrick Bar, sediment transport rates also increase effectively mobilizing the bed surface. Sand and fine gravel has a hydraulic smoothing effect, which can accelerate near bed velocities and mobilize gravel-sized particles (Ikeda, 1984; Venditti et al., 2010b). Depth-averaged velocities obtained in this study support this idea of changing bed roughness. During high flows, a velocity drop is observed near Sumas Mountain, and velocity observed downstream of Hatzic Bend is similar to velocity upstream of Sumas Mountain. During low flows this pattern is not observed in the results. This suggests that during peak flows a gravel load downstream of Yaalstrick bar is maintained, depositing into pools during low flows.

6: CONCLUSION

Building on work on the Fraser River gravel-sand transition by Venditti et al., (2008, 2010c) this study provides complementary flow and suspended-sediment transport data to observe sediment dynamics.

The spatial and temporal changes in flow and suspended sediment transport provide evidence to support the dominant control of the transition being a break in slope, which causes a loss of competence, as suggested by Mclean et al. (1999) and Venditti et al. (2008). A break in velocity can be seen just downstream of Sumas Mountain near the gravel-mine. This break is also observed in the shear stress values, SSC and sediment flux maps for all flows. This rapid decrease in flow and SSC in that area is also supported by LISST profiles, where a pronounced decrease in suspended-sediment concentration, suspended mean and median grain-size are seen near the gravel mine.

The flow and suspended-sediment transport results provide insight into the gravel-sand transition reach and suggest that sorting processes, caused by the loss of competence, control the abrupt gravel-sand transition. During low flows, conditions allow only very fine gravel to deposit downstream of Sumas Mountain and all sand is mobile in this reach. During high flows gravel greater than 8 mm is deposited downstream of Sumas Mountain. Sand stays in suspension during all flows and more sand is entrained downstream of Hatzic bend at higher flows. This causes maximum suspended-sediment concentrations

near Mission. During low flows a gravel load supplied by the gravel-bedded section upstream of Yaastrick Bar maintains the gravel front, and at high flows fine gravel escapes the gravel front and accumulates in pools and/or bar heads downstream of the break in slope.

It is clear that sediment supply influences the location of the transition. Without a constant sand supply the transition will not be able to maintain the sand-bedded section and the gravel front will in turn move downstream, which will change the location of the gravel-sand transition.

REFERENCE LIST

Bagnold, R.A. (1966). An approach to the sediment transport problem from general physics. *US Geol. Surv. Pap. 442-I.*

Brierley, G.J, & Hickin, E.J. (1985). The downstream gradation of particle sizes in the Squamish River, British Columbia. *Earth Surface Processes and Landforms, 10*, 597-606.

Campbell, I.A. (1970). Erosion rates in the Steveville Badlands, Alberta. *Canadian Geographer, 14*, 202-216.

Church, M. (1990). Fraser River in central British Columbia. In M.G. Wolman & H.C. Riggs (Eds.), *Surface-Water Hydrology, The Geology of North America* (pp. 282-287). Boulder, CO: Geological Society of America, Inc.

Church, M. (2007). Review of the lower Fraser River sediment budget: final report. Report to FREMP, 26 July, 2007: 24pp.

Deines, K. L. (1999). Backscatter estimation using broadband acoustic Doppler current profilers. *Proceedings of the IEEE Sixth Working Conference on Current Measurement*, *San Diego, CA*, 249-253.

Ferguson, R.I. (2003). Emergence of abrupt gravel to sand transitions along rivers through sorting process. *Geology, 31*(2), 159-162.

Ferguson, R., Hoey, T., Wathen, S., & Werrity, A. (1996). Field evidence for rapid downstream fining of river gravels through selective transport. *Geology, 24*(2), 179- 182.

Ferguson, R.I., Hoey, T.B., Wathen, S.J., Werritty, A., Hardwick, R.I., & Sambrook Smith, G.H. (1998), Downstream fining of river gravels: An integrated field lab and modeling study. In P. Klingeman et al., (Eds.), *Gravel-bed rivers in the environment: Proceedings of the 4th International Workshop on Gravel-bed Rivers* (pp. 85–114). Lakewood, Colorado: Water Resource Publications.

Gartner, J.W. (2004). Estimating suspended solids concentrations from backscatter intensity measured by acoustic Doppler current profiler in San Francisco Bay, California, *Marine Geology*, *211*,169-187.

Gomez, B., Rosser, B. J., Peacock, D. H., Hicks, D. M., & Palmer, J. A. (2001). Downstream fining in a rapidly aggrading gravel bed river, *Water Resour. Res.*, 37(6), 1813–1823, doi:10.1029/2001WR900007.

Ham, D.G. (2005). *Morphodynamics and sediment transport in a wandering gravel-bed channel: Fraser River, British Columbia*. Ph.D. thesis. University of British Columbia. Vancouver, BC.

Hickin, E.J. (1979). Concave-bank benches on the Squamish River, British Columbia, Canada, *Canadian Journal of Earth Sciences*, *16*, 200-203.

Howard, A.M. (1980). Thresholds in river regimes. In D. Coates & J. Vitek (Eds.), *Thresholds in Geomorphology* (pp.227-258). Boston: Allen and Unwin.

Ikeda, H. (1984). On the formation of stationary bars in a straight flume. *Annual Report to the Institute of Geoscience, Univ. Tsukuba*, *10*, 53-56.

Knighton, A. D. (1989). River adjustment to changes in sediment load: The effects of tin mining on the Ringarooma River, Tasmania, 1875–1984. *Earth Surface Processes and Landforms, 14,* 333–359. doi: 10.1002/esp.3290140408

Knighton, A. D. (1998). The gravel-sand transition in a disturbed catchment. *Geomorphology, 27,* 325-341.

Kodama, Y. (1994). Downstream changes in the lithology and grain size of fluvial gravels, the Waterase River, Japan: evidence of the role of abrasion in downstream fining. *Journal of Sedimentary Research, 64*(1), 68-75.

Kostaschuk, R., Best, J., Villard, P., Peakall, J., & Franklin, M. (2005). Measuring flow velocity and sediment transport with an acoustic Doppler current profiler. *Geomorphology, 68*(1-2), 25-37.

Mark, D.M., & Church, M. (1977). On the misuse of regression in earth science. *Mathematical Geology, 9*(1), 63-75.

McLean, D.G. (1990). *The relation between channel instability and sediment transport on lower Fraser River*. Ph.D. thesis. University of British Columbia, Vancouver.

McLean, D.G., Church, M., & Tassone, B. (1999). Sediment transport along lower Fraser River 1. Measurements and hydraulic computations. *Water Resources Research, 35*(8), 2533-2548.

Miller, M.C., McCave, I.N., & Komar, P.D., (1977). Threshold of sediment motion under uinidirectional currents. *Sedimentology*, 24, 507-527.

Paola, C., Parker, G., Seal, R., Sinha, S.K., Southard, J.B., & Wilcock, P.R. (1992). Downstream fining by selective deposition in a laboratory flume. *Science, 258,* 1757- 1760.

Paola, C., & Seal, R. (1995). Grain size patchiness as a cause of selective deposition and downstream fining. *Waster Resource Research, 31*(5), 1395-1407.

Pickup, G. (1984). Geomorphology of tropical rivers 1. Landforms, hydrology and sedimentation in the Fly and lower Purari, Papua New Guinea. *Catena Supplement, 5,* 1-17.

Reichel, G., & Nachtnebel, H.P. (1994). Suspended sediment monitoring in a fluvial environment: Advantages and limitations applying an acoustic Doppler current profiler. *Water Research, 28*(4), 751-761.

Rennie, C. D., & Church, M. (2010). Mapping spatial distributions and uncertainty of water and sediment flux in a large gravel bed river reach using an acoustic Doppler current profiler. *J. Geophys. Res.*, 115, F03035, doi:10.1029/2009JF001556.

Sambrook Smith, G.H., & Ferguson, R.I. (1995). The gravel-sand transition along river channels. *Journal of Sedimentary Research, 65*(2), 423-430.

Sambrook Smith, G.H., & Ferguson, R.I. (1996). The gravel-sand transition: flume study of channel response to reduced slope. *Geomorphology, 16,* 147-159.

Schaafsma, A.S. & Hay, A.E. (1997). Attenuation in suspensions of irregularly shaped sediment particles: A two- parameter equivalent spherical scatterer model*. J. Acoustical Society of America, 102*(3), 1485-1502.

Schulkin, M., & Marsh, H. W. (1962). Sound absorption in seawater, *J. Acoustical Society of America, 34*(6), 864-865.

Seal, R., & Paola, C. (1995). Observations of downstream fining on the North Fork Toutle River near Mount St. Helens, Washington. *Water Resources Research, 31*(5), 1409-1419.

Shaw, J., & Kellerhals, R. (1982). The composition of recent alluvial gravels in Alberta River beds. *Alberta Research Council Bulletin, 41,* 151.

Sibson, R. (1981). Chapter 2: A Brief Description of Natural Neighbor Interpolation. In *Interpolating multivariate data* (pp. 21–36). New York: John Wiley & Sons.

Sichingabula, H.M. (1993). *Character and controls of suspended-sediment concentration and discharge effectiveness, Fraser River, British Columbia.* Ph.D. thesis. Simon Fraser University. Burnaby, BC.

Sime, L. C., Ferguson, R. I., & Church, M. (2007). Estimating shear stress from moving boat acoustic Doppler velocity measurements in a large gravel bed river, *Water Resour. Res.*, 43, W03418, doi:10.1029/2006WR005069.

Singer, M.B. (2008). Downstream patterns of bed-material grain size in a large, lowland alluvial river subject to low sediment supply, *Water Resources Research*, 44, W12202, doi: 10.1029/2008WR007183.

Singer, M.B. (2010). Transient response in longitudinal grain size to reduced gravel supply in a large river, *Geophysical Research Letters,* 37, L18403, doi:10.1029/2010GL044381.

Thevenot, M. M., Prickett, T. L., Kraus, N. C.(1992). Tylers Beach, Virginia, dredged material plume monitoring project 27 September to 4 October 1991, Dredging Research Program Technical Report DRP-92-7, Washington: US Army Corps of Engineers.

Thorne, P.D., Vincent, C.E., Hardcastle, P.J., Rehman, S., & Pearson, N. (1991). Measuring suspended sediment concentrations using acoustic backscatter devices. *Marine Geology*, *98*(1), 7-16.

Topping, D.J., Melis, T.S., Rubin, D.M., & Wright, S.A. (2004). High-resolution monitoring of suspended-sediment concentration and grain size in the Colorado River in Grand Canyon using a laser-acoustic system. *Proceedings of the Ninth International Symposium on River Sedimentation, Yichang, China*, People's Republic of China: Tsinghua University Press, 2507-2514.

Topping, D. J., Wright, S.A., Melis, T.S., and Rubin, D.M. (2007). High-resolution measurement of suspended- sediment concentrations and grain size in the Colorado River in Grand Canyon using a multi-frequency acoustic system, *Proc. 10th International Symposium on River Sedimentation*, Moscow, Russia, v. 3, 330- 339.

Van Rijn, L.C. (1984) Sediment transport, part III: bed forms and alluvial roughness. *J. Hydraul. Eng., ASCE, 110,* 1733-1754.

Venditti, J. G., Dietrich, W. E., Nelson, P. A., Wydzga, M. A., Fadde, J., & Sklar, L. (2010a). Effect of sediment pulse grain size on sediment transport rates and bed mobility in gravel bed rivers, J. Geophys. Res., 115, F03039, doi:10.1029/2009JF001418.

Venditti, J. G., Dietrich, W. E., Nelson, P. A., Wydzga, M. A., Fadde, J., & Sklar, L. (2010b). Mobilization of coarse surface layers in gravel-bedded rivers by finer gravel bed load, *Water Resour. Res.*, 46, W07506, doi:10.1029/2009WR008329.

Venditti, J.G., Humphries, R.P., Allison, M.A., Nittrouer, J.A., Church, M. (2008). Gravel- sand transition in a large, lowland alluvial channel, Eos Trans. AGU, *89*(53), Fall Meet. Suppl., Abstract H52C-05.

Venditti, J.G., Humphries, R.P., Allison, M.A, Nittrouer, J.A. & Church, M. (2010c). Morphology and dynamics of a gravel-sand transition. *Proceedings of the 9th Federal Interagency Sedimentation Conference*, Las Vegas, NV

Wall, G.R., Nystrom, E.A., & Litten, S. (2006). Use of an ADCP to compute suspended- sediment discharge in the tidal Hudson River, New York, *U.S. Geological Survey Scientific Investigations Report 2006-5055*.

Watson, D. (1992). *Contouring: A Guide to the Analysis and Display of Spatial Data*, London: Pergamon Press.

Wilcock, P.R. (1998). Two-fraction model of initial sediment motion in gravel-bed rivers. *Science, 280,* 410-412.

Wilcock, P.R., & Kenworthy, S.T. (2002). A two‐fraction model for the transport of sand/gravel mixtures, Water Resour. Res., 38: 1194, doi:10.1029/2001WR000684.

Wilcock, P.R., Kenworthy, S.T., & Crowe J.C. (2001). Experimental study of the transport of mixed sand and gravel. *Water Resources Research, 37*, 3349-3358.

Wilcock, P. R., & McArdell, B. W. (1997). Partial transport of sand/gravel sediment, *Water Resour. Res.*, *33*(1), 235–245.

Wright, S. A., Topping, D. J., Rubin, D. M., & Melis, T. S. (2010). An approach for modeling sediment budgets in supply-limited rivers, *Water Resour. Res.*, 46, W10538, doi:10.1029/2009WR008600.

Yalin, M. S., & Karahan, E. (1979). Inception of sediment transport. *J. Hydraul. Div. -ASCE, 105*(11), 1433–1443.

Yatsu, E. (1955). On the longitudinal profile of the graded river. *American Geophysical Union Transactions, 36,* 655-663.